Flow in Heterogeneous Porous Media: Implications for Geological Carbon Storage

Waterton, Pedro

Flow in Heterogenous Porous Media: Implications for Geological Carbon Storage

P.C. Waterton, Emmanuel College

January 6, 2012

Supervised by
Jerome Neufeld & Mike Bickle

Word Count: 7409

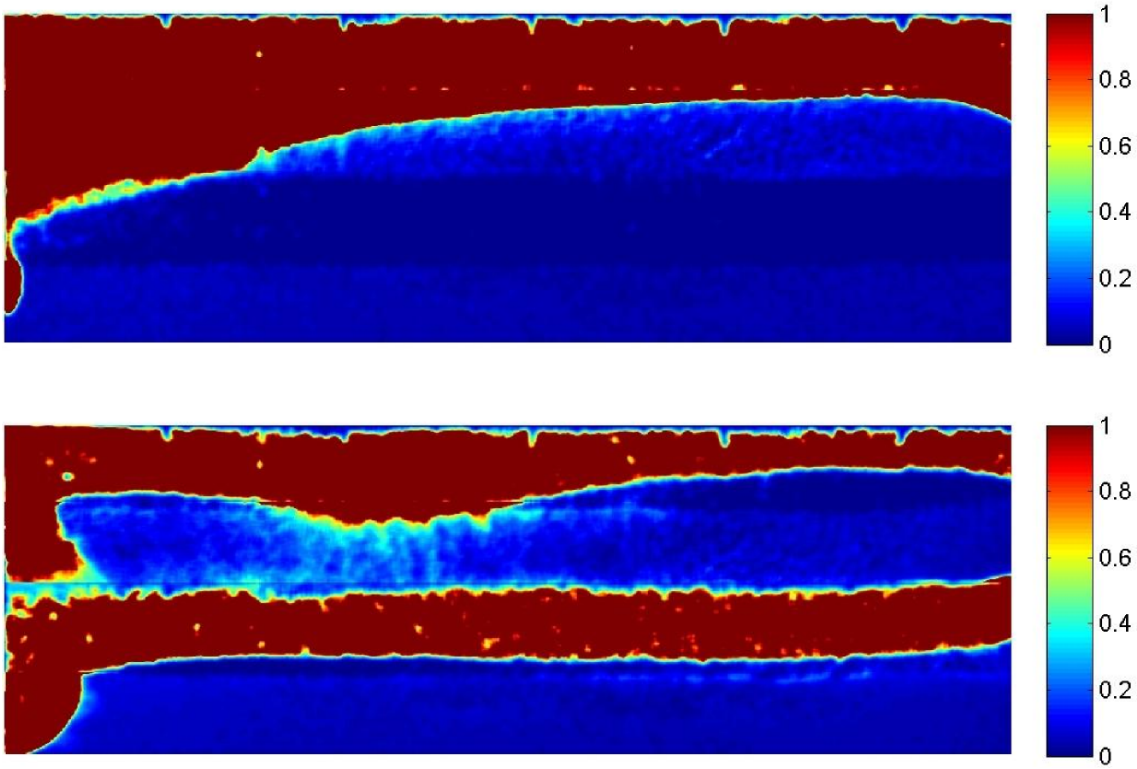

Abstract

Experiments investigating the flow of two fluids in an approximately 2D heterogenous porous medium are combined with 1D mathematical analysis with a view to understanding the dissolution of CO_2 in reservoir brines in an enhanced oil recovery (EOR) geometry. The model adequately describes many aspects of the flow observed in experiments when gravity can be ignored, and can explain some aspects of the flow developed when gravity is important. The growth and retreat of pore scale viscous fingers was observed, driven by significant cross-layer pressure differences predicted by the model. These fingers significantly increase the interfacial area between fluids with a viscosity contrast in a heterogenous medium, and are thought to enhance CO_2 dissolution in reservoir brines. Two flow regimes are observed when gravity acts perpendicular to the principal direction of flow, one in which flow is by controlled by density differences and a second in which flow is focussed along high permeability layers. The second regime is predicted to allow the most mixing between fluids, and is calculated to occur in typical EOR situations.

Contents

1 Introduction

The concentration of atmospheric CO_2 increased from the pre-industrial value of 280ppm to 379ppm during the 250 years leading up to 2005, compared to an increase of only 20 ppm over the 8000 years prior to industrialisation. Anthropogenic fossil fuel use, agriculture and land use changes have been the dominant causes of this increase. It is very likely (>90% likelihood) that the main cause of an observed global temperature increase of 0.76°C in the past 150 years is the increase in atmospheric concentrations of greenhouse gases, such as CO_2 [Solomon et al., 2007].

With power production from fossil fuels accounting for 55% of anthropogenic CO_2 emissions, further increases in the atmospheric concentration of CO_2 and their potentially damaging climactic effects could be mitigated by capturing CO_2 at the power plant and storing it [Bickle, 2009]. Several different mechanisms have been proposed for long term storage of CO_2 once captured at source, including: storage in coal beds by adsorption onto organic materials [Bachu, 2008]; injection of CO_2 charged water into reactive rock formations such as basalts [Alfredsson et al., 2008] and enhancing natural rates of carbonation of exposed peridotites [Kelemen and Matter, 2008].

However, the currently best understood and most developed method for geological CO_2 storage is in depleted oil and gas reservoirs or saline aquifers. Depleted oil and gas reservoirs combined with deep saline formations are likely to have some of the largest potential for long term storage [Johnson and Santillo, 2003], and large natural accumulations of CO_2 and natural gas already exist stably in such situations [Gilfillan et al., 2008]. The technology to compress and inject CO_2 into geological formations has been developed by the oil and gas industry over the past 35 years for use in enhanced oil recovery (EOR), with over 13,000 CO_2 EOR wells in the U.S.A. alone [Meyer, 2007].

Geological Context

EOR involves the injection of substances, including CO_2, that alter the chemical properties of the oil to increase oil production. Some of the injected CO2 is produced together with the oil and, after separation, may be re-injected. EOR projects using CO_2 are relevant to CO_2 sequestration, as they both provide a financial incentive for further research into CO_2 technology, and as a significant proportion (simulations suggest up to 66%) of the injected CO_2 may remain in the reservoir [Holt et al., 1995].

Salt Creek is a mature onshore oil field in Wyoming, USA, which has been subject to CO_2 flooding since 2004. The EOR program at Salt Creek is one of the largest CO_2 sequestration projects in the world, with net storage of 2.2Mt CO_2 equivalent per year [Grygar and Schmults, 2009]. The main reservoir formation at Salt Creek (Wall Creek 2) is believed to be laterally homogenous, but shows large vertical variations in permeability. Supercritical CO_2, that is less dense and less viscous than the ambient fluids is injected

in a five spot pattern, with spacings of around 200m between injection and production wells. A reservoir thickness of approximately 25m, comparable to the seismic tuning thickness, means that seismic surveys cannot establish the detailed nature of the flow [O'Brien et al., 2010].

The amount of CO_2 that dissolves in the ambient fluids at sites like Salt Creek will depend on the nature of the CO_2 flow developed within the reservoir, and is important as solubility trapping of CO_2 is considered one of the primary mechanisms for ensuiring stable long term storage of CO_2 [Neufeld et al., 2010].

Geochemical data from an injection experiment at Salt Creek starting in September 2010 observed significant dissolution of CO_2 in brines. 2D flow modelling suggests that the flow of CO_2 would be strongly controlled by the heterogenous permeability structure of the reservoir, and that flow of brines adjacent to the highest permeability layers filled with CO_2 could cause the observed dissolution of CO_2 [Bickle et al., 2011]. Viscous fingering of the CO_2 (see §3.1) may also be important as it is expected to cause a large increase in the surface area of the contact between the CO_2 and the brines, increasing the rate at which the CO_2 dissolves in the brine.

Project Aims

To investigate such permeability-controlled flow and the extents of flow between layers a series of experiments were carried out coupled with mathematical analysis based on analytical solutions for 1D displacement in a many-layered porous medium. Some key questions are:

- How does the permeability structure control the flow of the injected CO_2 within the reservoir?
- How important is flow perpendicular to the layers and can it explain the observed dissolution of CO_2 at Salt Creek?
- What effect does viscous fingering have on the dissolution of CO_2 in brines?

The experimental arrangement is described in §2, and the development of the 1D analytical theory to accompany the experiments is presented in §3. The calibration required for data collection and analysis is explained in §4, with the results and analysis of the experimental data presented in §5. A discussion of the results and some of the possible implications of this work is given in §6, with the major conclusions listed in §7.

2 Experimental Equipment

A great number of simplifications were needed to try and understand the underlying physics controlling a complex geological system. To facilitate data collection in the form of photographs, the tank had to be approximately two dimensional, so that the implicit depth average taken in a photograph through a fluid provides reasonably representative results for the experimental flows. The real world reservoir was approximated by a closed, narrow (1cm thick) perspex tank. A heterogenous permeability structure was formed by layering spherical glass ballotini of different sizes (figure 1). Ballotini of diameter 3 mm and 1 mm were packed into the cell in alternating layers to create beds of high and low permeability. The Carman-Kozeny model for the permeability of random packed spheres predicts

$$k = \frac{\phi^3 d^2}{180(1-\phi)^2}, \tag{1}$$

where k is the permeability, ϕ is the porosity and d is the diameter of the beads. Thus, for similar packing the 3 mm bead layers should be almost an order of magnitude more permeable than the 1 mm bead layers.

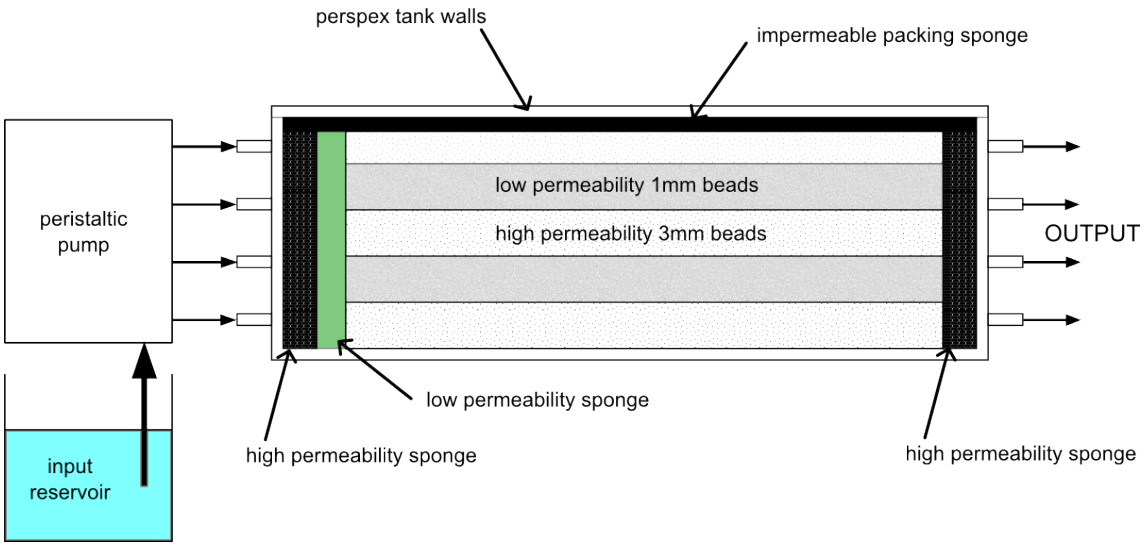

Figure 1: Schematic diagram of the tank used for the experiments.

The tank was flooded with fluid, either water or glycerin, to represent the ambient fluid in a real reservoir. A second, dyed fluid, either water or an NaCl solution, representing the injected CO_2, was injected at a constant volume flux through four input nozzles using a peristaltic pump. Four more output nozzles allowed fluid to leave the tank at the far end at roughly atmospheic pressure. These inputs and outputs are intended to represent injection and production wells in the reservoir.

High permeability sponge layers were inserted at either end of the tank to ensure

pressure is equalised upon entry and exit from the medium. The low permeability sponge was added to help produce a linear fluid interface upon entry from the four point inputs.

The injected fluid mass flux was measured by logging the mass of an input fluid reservoir using a mass balance. The tank was lit from behind and flow data was collected by photographing the tank at regular intervals using a digital camera, with the dye in the injected fluid acting as a tracer.

The dimensions of the tank along with errors as used for calculations are shown in table 1.

Parameter	Value
Length (of porous medium)	51.7 ± 0.1 cm
Width of layers 1-4	4 ± 0.5 cm
Width of layer 5	2.8 ± 0.5cm
Tank Thickness	1.155 ± 0.155cm
Porosity of 3 mm beads	0.44
Porosity of 1 mm beads	0.4
Permeability of 3 mm beads	1.36×10^{-4}
Permeability of 1 mm beads	1.20×10^{-5}

Table 1: Layer 5 was narrower than the others due to the presence of the packing sponge. Large errors in the layer widths were introduced by compaction, which occured in most experiments after the tank was sealed. Errors in tank thickness largely arose from outwards bowing of the tank walls when filled, leading to a greater thickness in the centre of the tank than the ends. Permeabilities and porosities used are those measured for 3 mm and 1 mm glass ballotini in a 1cm thick tank [Strandkvist et al., prep].

3 Theory

3.1 Saffmann-Taylor Instability

The viscosity difference between the injected CO_2 and water is expected cause viscous fingering of the CO_2, known as the Saffman-Taylor instability. This instability may occur when a fluid displaces another, more viscous fluid in a porous medium. The cause of this instability can be understood by considering the displacement of an interface between two fluids, A and B, with viscosities μ_A and μ_B, and densities ρ_A and ρ_B (see figure 2).

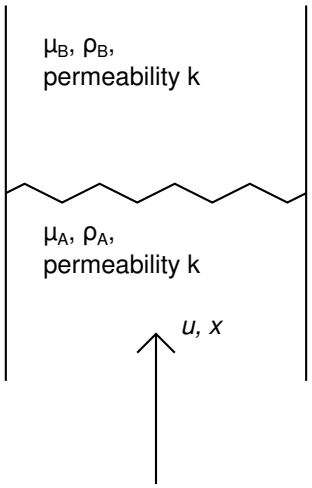

Figure 2: Displacement of fluid B by fluid A, separated by an interface across which the density and viscosity vary rapidly (sharp interface).

In a porous medium the fluid motion can be described by Darcy's law, which in one dimension with the effects of gravity included can be written

$$\frac{\partial P}{\partial x} = \frac{\mu u_x}{-k} + \rho g_x. \tag{2}$$

The pressure force $(P_A - P_B)$ on the displaced fluid as a result of a displacement, δx, of the interface is

$$\delta P = P_A - P_B = [\frac{u(\mu_B - \mu_A)}{k} + g(\rho_A - \rho_B)]\delta x. \tag{3}$$

If δP is positive, then any small displacement will amplify, leading to an instability [Homsy, 1987]. In the case of geological CO_2 storage, where the CO_2 injected is less viscous than the brine or oil that it displaces, the Saffman-Taylor instability will always occur for horizontal displacements.

This instability causes the interface to deform into branching fingers over a variety of length scales (figure 3). However, in sediments, and in the heterogenous medium used in the experiments the fingering is likely to be controlled by the large changes in permeability between beds.

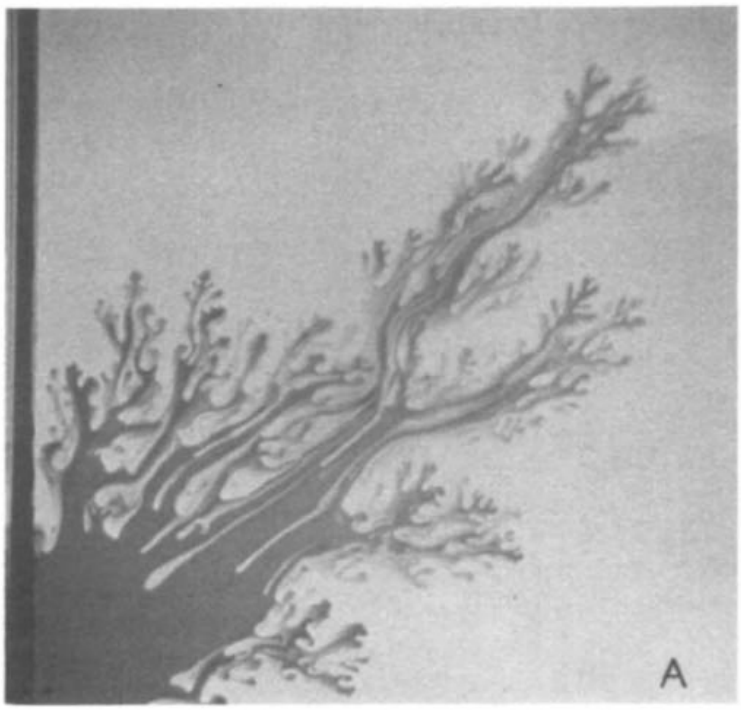

Figure 3: Miscible flow in a five-spot geometry showing viscous fingering, observed in a Hele-Shaw cell. Taken from Homsy, 1987.

3.2 1D Analytical Theory

We consider a closed tank filled by a porous medium with parallel layers of varying permeability (as illustrated in figure 4). The tank is rectangular and assumed to be two dimensional, with length L in the x direction. The layers are parallel to x. Each layer i, of cross sectional area perpendicular to x, a_i, and width, w_i, has porosity ϕ_i and permeability k_i.

The tank is wholly saturated with fluid B, of viscosity μ_B and density ρ_B. Fluid A, of viscosity μ_A and density ρ_A is injected into the tank at a constant mass flux, Q. The injection is from a linear source perpendicular to the layers at pressure P_0. Fluid leaves the tank via a linear outlet, across which the pressure equalises at P_1. The volume of fluid in the tank is conserved.

An abrupt interface between fluid A and fluid B is assumed in each layer, with position ξ_i in layer i. The pressure at this interface is $P_{\xi i}$. The flow perpendicular to the length of the tank is assumed to be negligible compared to the flow parallel to the length of the tank (and so the flow is treated as one dimensional in each layer). Gravity is ignored (x and z horizontal) and it is assumed that fluid A and B are miscible.

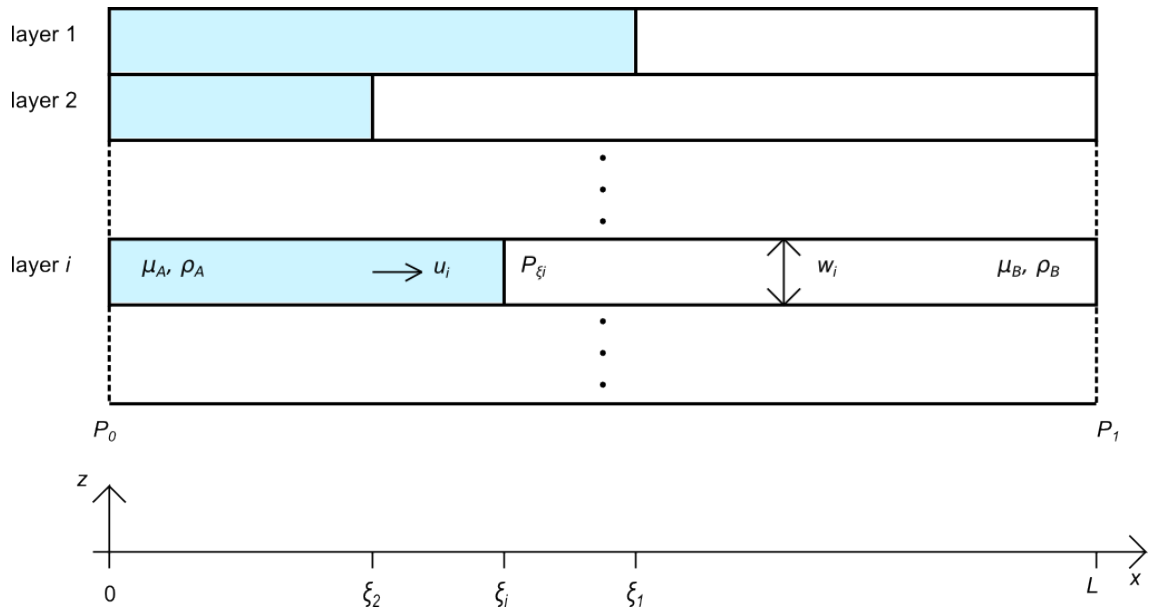

Figure 4: Diagram of the theoretical tank used for calculations. Fluid A is coloured blue for clarity. The positions of the interfaces shown are for $k_1 > k_i > k_2$

.

3.2.1 Driving Pressure and Interface Velocities

The following derivation is based on 1D displacement of two fluids in a single layer [Bear, 1972]. Fluid flow in a porous medium is governed by Darcy's Law:

$$u = \frac{-k}{\mu}\frac{\partial P}{\partial x} \tag{4}$$

where u is the velocity of the fluid, k is the permeability, μ is the viscosity, and $\frac{\partial P}{\partial x}$ is the pressure gradient in the direction of flow, x.

In practice, experiments were conducted by injecting a known (measured) mass flux by means of a peristaltic pump. Therefore, to compare experiments with theoretical predictions this mass flux must be translated into appropriate pressure gradients.

The fluids in the tank are assumed to be incompressible and so the volume of fluid in the tank is conserved. This can be written $\nabla \cdot \underline{u} = 0$, where $\underline{u}$ is the flow velocity. For a 2D tank where flow in the z direction has been assumed to be negligible, $\frac{\partial u}{\partial x} = 0$, or the velocity in the x direction is constant.

As the velocity is roughly constant, the pressure gradient should also be constant in each fluid where μ is constant. For $\mu_A < \mu_B$ the pressure gradient in layer i is given by

$$\left.\frac{\partial P}{\partial x}\right|_A = \frac{P_{\xi i} - P_0}{\xi_i}, \tag{5}$$

$$\left.\frac{\partial P}{\partial x}\right|_B = \frac{P_1 - P_{\xi i}}{(L - \xi_{i)}}, \tag{6}$$

as shown in figure 5.

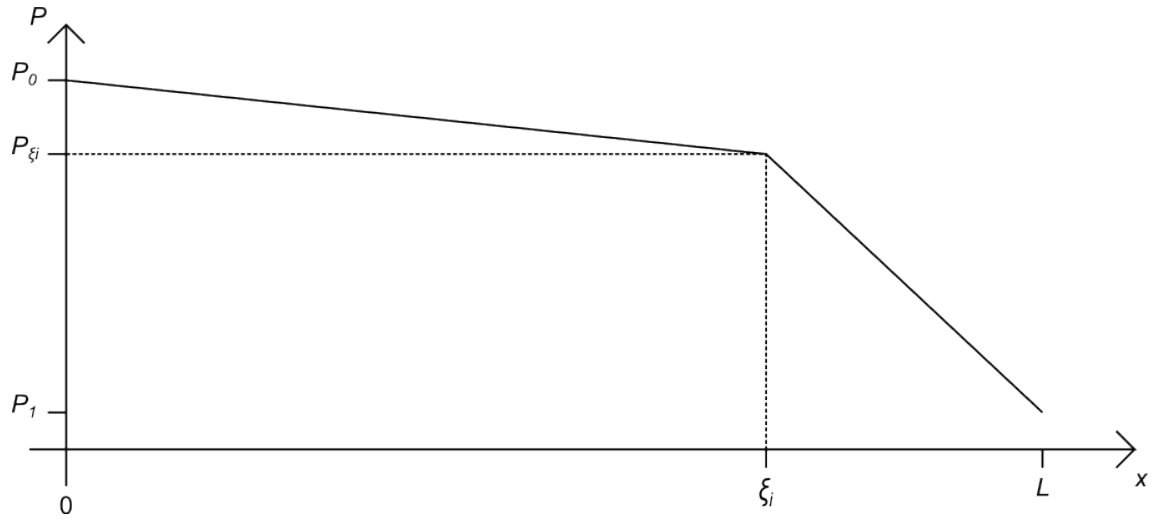

Figure 5: Pressure along length of layer i for $\mu_A < \mu_B$. At a constant velocity the pressure gradients in fluids A and B will be constant but from Darcy's law the gradient will be steeper in the fluid with higher viscosity.

The flow velocity in each region is therefore

$$u_{iA} = \frac{-k_i}{\mu_A}\frac{P_{\xi i} - P_0}{\xi_i}, \tag{7}$$

$$u_{iB} = \frac{-k_i}{\mu_B}\frac{P_1 - P_{\xi i}}{L - \xi_i}, \tag{8}$$

where u_{iA} and u_{iB} are the velocities in fluid A and B in layer i. These must be equal if volume is conserved ($u_{iA} = u_{iB} = u_i$), and are also the speed at which the interface between the fluids moves. Equating $P_{\xi i}$ and rearranging gives

$$P_0 - P_1 = \Delta P = \frac{u_i}{k_i}(\mu_B(L - \xi_i) + \mu_A \xi_i). \tag{9}$$

The relationship between the fluid velocity, u_i, and mass flux, q_i, entering each layer is given by

$$u_i = \frac{q_i}{a_i \phi_i \rho_A}, \tag{10}$$

and so the mass flux through each layer is

$$q_i = \frac{\Delta P a_i \phi_i \rho_A k_i}{\mu_B(L - \xi_i) + \mu_A \xi_i}. \tag{11}$$

The total mass flux, Q, entering the tank is the sum of the mass fluxes entering each of the individual layers

$$Q = \sum_i q_i = \Delta P \rho_A \sum_i \frac{a_i \phi_i k_i}{\mu_B (L - \xi_i) + \mu_A \xi_i}, \tag{12}$$

and so the pressure change across the tank, ΔP, is given

$$\Delta P = \frac{Q}{\rho_A \sum_i \frac{a_i \phi_i k_i}{\mu_B (L - \xi_i) + \mu_A \xi_i}}. \tag{13}$$

This can be simplified slightly by replacing ξ_i with the dimensionless length, ζ_i, where $\zeta_i = \frac{\xi_i}{L}$. This gives the pressure change across the tank as

$$G = \frac{\Delta P}{L} = \frac{Q}{\rho_A \sum_i \frac{a_i \phi_i k_i}{\mu_B (1 - \zeta_i) + \mu_A \zeta_i}}. \tag{14}$$

At a constant tank thickness, d, and layer widths, w_i, the a_i can be replaced by $a_i = w_i d$. Allowing the width of the layers to tend to zero and the number of layers to tend to infinity returns

$$G = \frac{\Delta P}{L} = \frac{Q}{\rho_A d \int \frac{\phi(z) k(z)}{\mu_B (1 - \zeta(z)) + \mu_A \zeta(z)} dz} \tag{15}$$

where $\phi(z)$, $k(z)$ and $\zeta(z)$ are the distributions of porosity, permeability and interface position in the y direction.

It is clear that the pressure change across the tank will depend on the position of the position of the fluid interfaces in the tank. However, in the special case where $\mu_A = \mu_B = \mu$ the pressure gradient will not depend on interface position and will be the same the same at all points in the tank

$$G = \frac{\Delta P}{L} = \frac{Q \mu}{\rho_A \sum_i \phi_i a_i k_i}. \tag{16}$$

Using this pressure gradient and Darcy's law gives the fluid velocity in each layer

$$u_i = \frac{k_i Q}{\rho_A \sum_i \phi_i a_i k_i} \tag{17}$$

Away from this special case, it has already been stated that as a result of conservation of volume and neglecting flow perpendicular to x, the u_i are constant. Therefore the interface velocities can be found by evaluating at a single set of interface positions, ξ_i. At the start of injection all of the $\xi_i = 0$ and so (13) becomes

$$\Delta P = \frac{Q}{\rho_A \sum_i \frac{a_i \phi_i k_i}{\mu_B L}}. \tag{18}$$

With the $\xi_i = 0$, equation 9 becomes

$$\Delta P = \frac{u_i \mu_B L}{k_i}. \tag{19}$$

Equating these and rearranging returns the same expression for velocities in each layer as in the single viscosity case (equation 17).

3.2.2 Interface Pressures

If the assumptions of predominantly 1D flow are valid, constant pressure gradients in the tank mean the only information required to calculate the pressure at all points in a layer will be P_0, P_1 and the position and pressure at the interface, ξ_i and $P_{\xi i}$. From Darcy's law

$$\left.\frac{\partial P}{\partial x}\right|_A = \frac{-u_{iA}\mu_A}{k_i}, \tag{20}$$

$$\left.\frac{\partial P}{\partial x}\right|_B = \frac{-u_{iB}\mu_B}{k_i}. \tag{21}$$

Combining with equations 5 and 6, and remembering that $u_{iA} = u_{iB}$,

$$\frac{\left.\frac{\partial P}{\partial x}\right|_A}{\left.\frac{\partial P}{\partial x}\right|_B} = \frac{\mu_A}{\mu_B} = \frac{1}{M} = \frac{(P_{\xi i} - P_0)(L - \xi_i)}{\xi_i (P_1 - P_{\xi i})}, \tag{22}$$

where $M = \frac{\mu_B}{\mu_A}$ is the mobility ratio. By again non-dimensionalising the interface postions ($\zeta_i = \frac{\xi_i}{L}$), and rearranging, the interface pressure, $P_{\zeta i}$, is given

$$P_{\zeta i} = \frac{P_0 M(1 - \zeta_i) + P_1 \zeta_i}{M(1 - \zeta_i) + \zeta_i}. \tag{23}$$

This can be simplified if pressures are measured relative to the output pressure, P_1. This gives $P_1' = 0$, $P_0' = P_0 - P_1 = \Delta P$ and $P_{\zeta i}' = P_{\zeta i} - P_1$, so equation 23 can be rewritten

$$\frac{P_{\zeta i}'}{\Delta P} = \frac{M(1 - \zeta_i)}{M(1 - \zeta_i) + \zeta_i}. \tag{24}$$

A plot of dimensionless interface pressure ($\frac{P_{\zeta i}'}{\Delta P}$) against dimensionless interface postion (ζ_i), at varying mobility ratios is given in figure 6

This variation in interface pressure with position is expected to cause pressure gradients perpendicular to the layers across two adjacent layers with different interface positions.

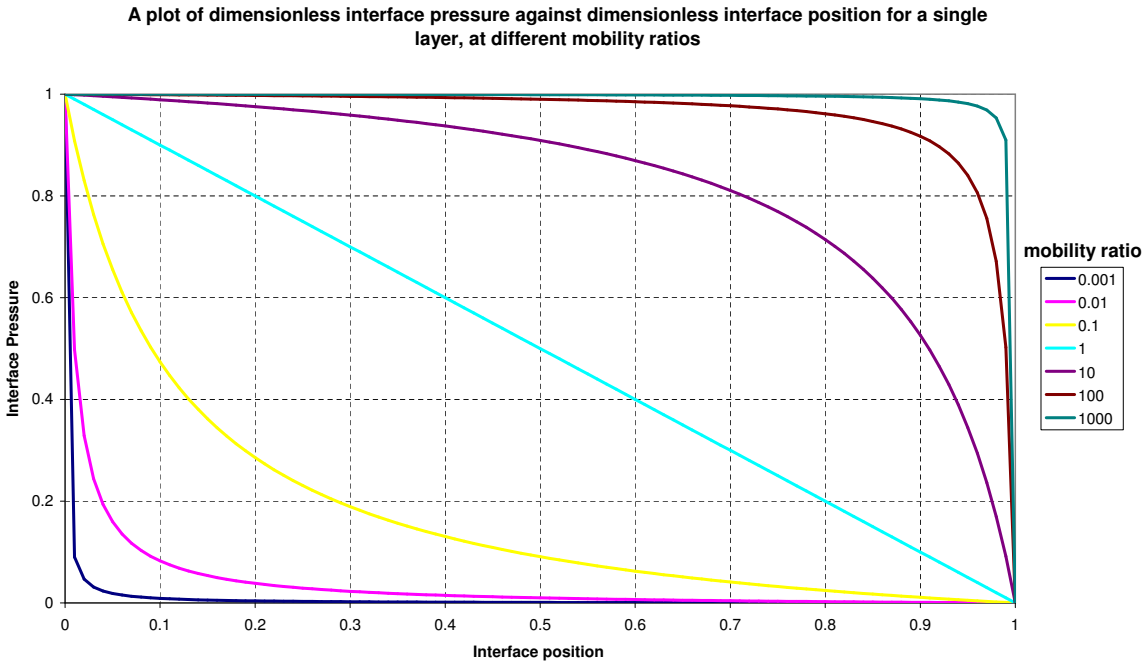

Figure 6: Plots of dimensionless interface position against diensionless interface position at varying mobility ratio, M. For $M > 1$, the injected fluid is less viscous, and for $M < 1$ it is more viscous than the fluid it displaces.

4 Calibration

4.1 Pressure Gradient

It was first necessary to demonstrate that a constant pressure gradient across the width of the cell in the absence of varying permeability and fluid properties. This was tested visually by packing the cell entirely with 3 mm beads and injecting dyed water into the water-flooded tank. The fluid velocity in the tank was observed from the progress of the dyed water front across the tank. For Darcy flow, a constant velocity across the width of the cell demonstrates a constant pressure gradient.

An uneven dye front was observed when using pure water, which appeared to be due to the dye input to the porous medium being initially uneven. The dyed water was allowed form a straight interface before entering the porous medium by adding a small quantity of salt (1.45 wt% NaCl) to the injected water, giving a density of 1.0084g cm^{-3} [Weast, 1985]. Some dyed water was then pumped into the tank with the tank tilted at an angle, and the pumped turned off. The higher density of the injected water forced the formation of a straight interface, stabilised by gravity, behind the low permeability sponge in the tank. The tank was then returned to horizontal and the pump restarted. A uniform interface perpendicular to the length of the tank was observed (figure 7).

This initial gravity stabilisation of the interface was used before for all further experiments with the tank in a horizontal orientation.

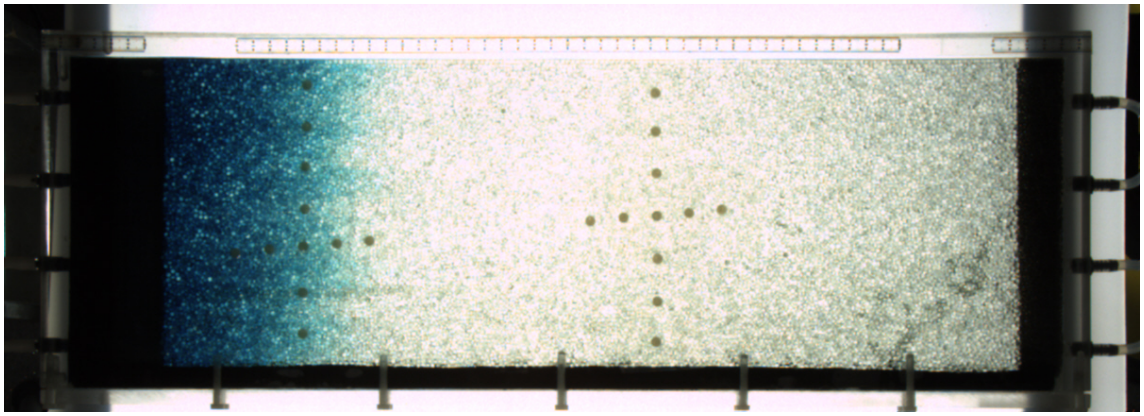

Figure 7: Raw image showing the advance of the dyed water interface 170 s after injection began at a mass flux of 0.4420 gs^{-1}. The straight interface observed demonstrates an apporximately constant pressure gradient across the width of the tank.

4.2 Concentration Calibration

A series of calibration experiments were required to convert colour intensities of photographs taken during experiments to concentrations of injected fluid. Separate calibrations were required for the horizontal and vertical experiments as different lightsources were used. The tank was flooded with dyed water of known concentration of dye. This flooding was allowed to continue until the colour intensities in representative patches from both the high and low permeability layers stopped changing (figure 8).

Uneven backlighting was a problem as this lead to different measured intensities even at constant dye concentration. This was especially a problem in the experiments with the tank orientated horizontally as a specialised light bank was unavailable (figure 9).

To correct for this long wavelength intensity variation, each image was subtracted from an un-dyed reference image, both in the calibration experiments and for all further image processing (figure 10). This also prevents negative concentration values from being measured in the middle of the tank where the light intensity is brightest.

A Matlab script (§D.1)was then used to average the RGB colour intensities across all of the high and low permeability parts of the tank to plot a relationship between dye concentration and colour intensity. The recorded points were fitted with exponential curves. Separate relationships were required for the low and high permeability layers due to the different optical properties of the different sized beads.

To improve the accuracy of concentration measurements, the RGB channel with the greatest dynamic range (range of concentrations over which intensity varies significantly) was chosen. The plots in figure 11 show that the blue colour channel has the greatest dynamic range.

It was then tested that the intensity-concentration data did not vary significantly between layers with the same size of beads used, to ensure that an average intensity-

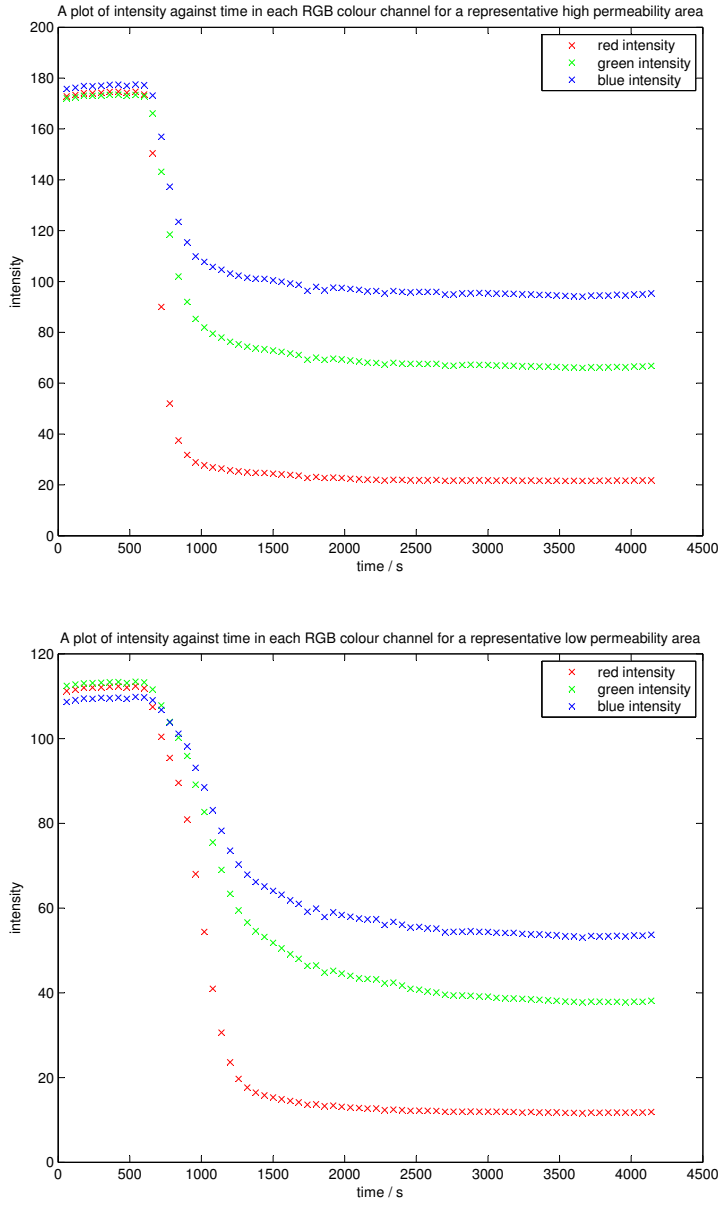

Figure 8: Intensity-time plots from representative areas from a horizontal calibration experiment in which the tank, initially filled with un-dyed water was flooded with water with a dye concentration of 0.2 vol%. Representative areas were chosen at the end of the tank furthest from the inputs so that when the intensity stops changing, the tank can be assumed to be filled entirely with 0.2 vol% dyed water.

concentration curve could be used (figure 12).

Dye concentrations were determined from measured blue intensities, using the average relationships in figures 13 and 14.

The dye concentration in the injected fluid was chosen to be 0.5 vol% (or 5ml dye per l water) for all further experiments, as the colour intensity begins to saturate beyond this point.

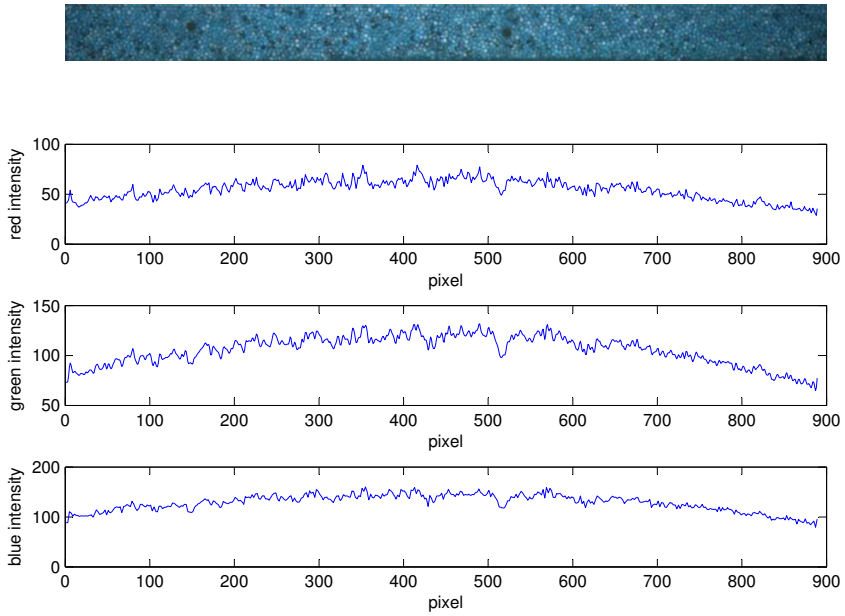

Figure 9: Cropped raw image of a high permeability layer flooded with 0.1 vol% dye concentration during a horizontal calibration experiment, along with width-averaged intensity profiles for each RGB channel. The intensities measured are higher in the centre of the tank than at the edges. This would lead to misleading concentrations measurements when an averaged concentration-intensity relationship is used.

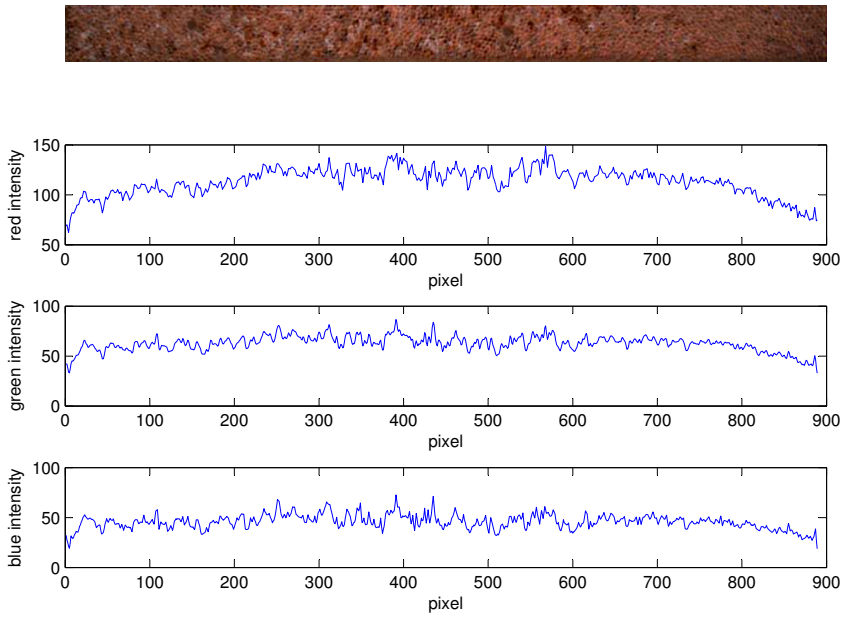

Figure 10: Cropped image of a high permeability layer from a horizontal calibration experiment flooded with 0.1 vol% dye concentration, following subtraction from an undyed reference image. Width-averaged intensity profiles for each RGB channel are also shown. Though the signal to noise ratio is worse following subtraction, the long wavelength intensity variation is largely removed except at the very ends of the tank. The relative noise increase can be dealt with using smoothing operations in later processing.

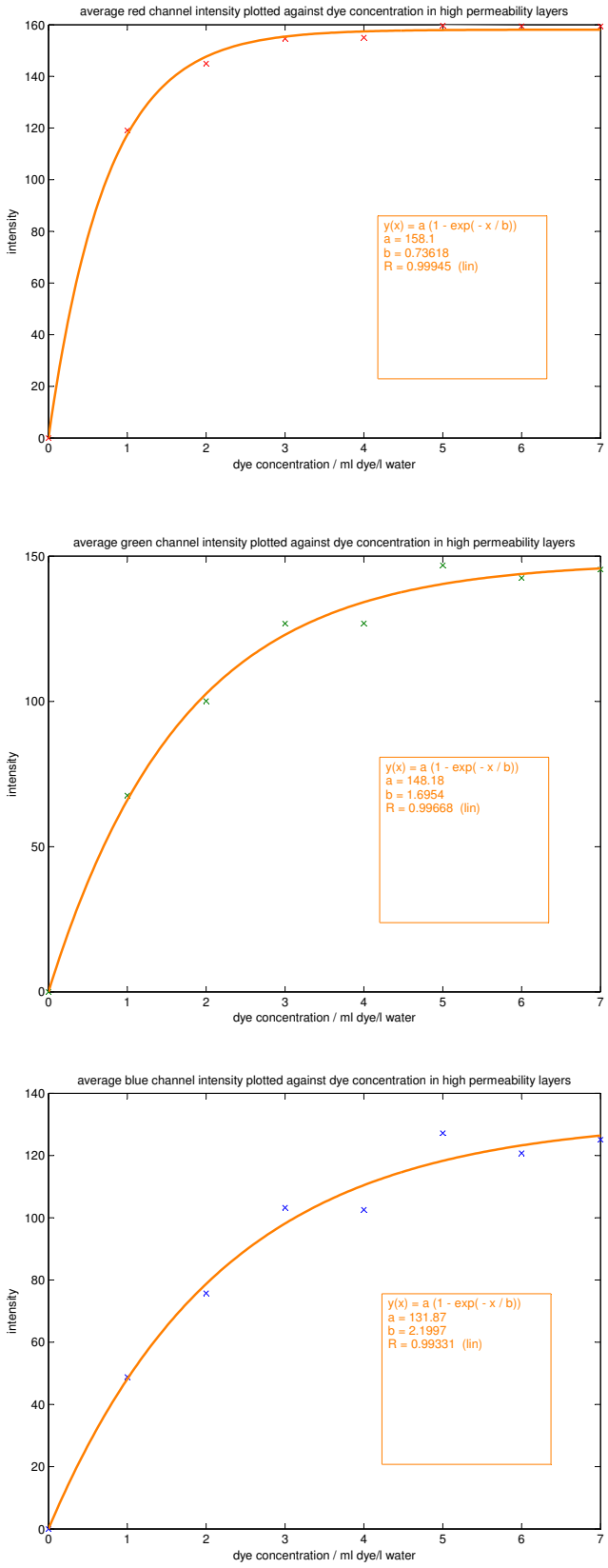

Figure 11: Intensity-concentration plots for each RGB channel for the horizontal calibration experiments. The blue channel has the largest dynamic range (largest 'b' value in the fitted curves).

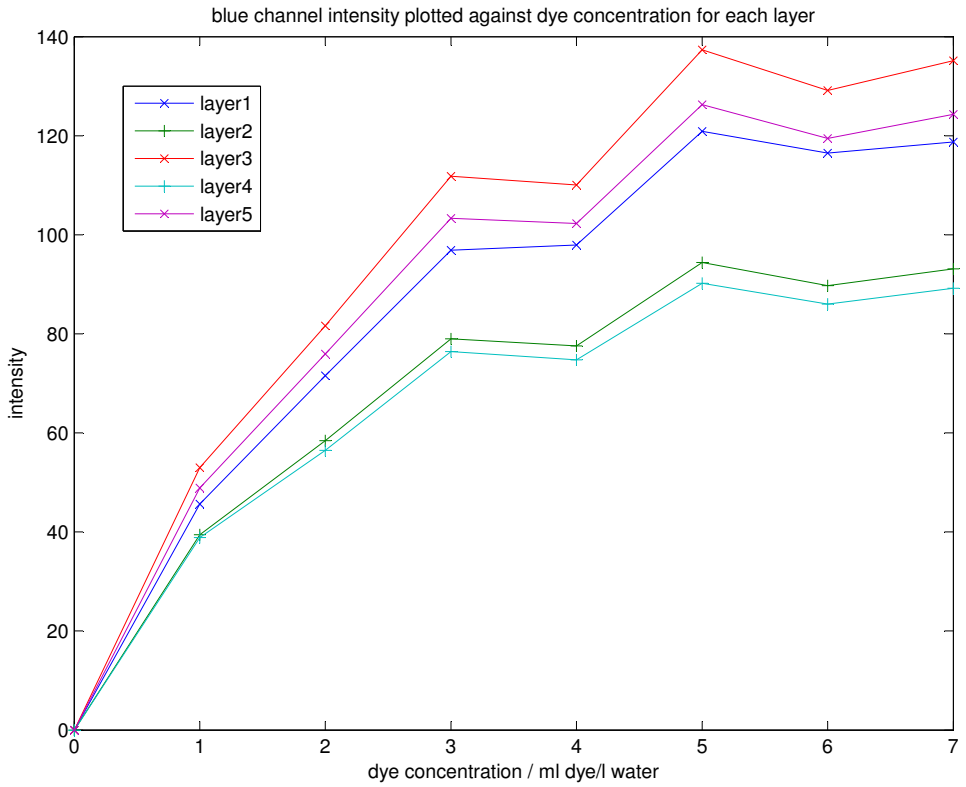

Figure 12: Blue channel intensity against concentration for each individual layer from the horizontal calibration experiments. High permeability layers are marked with 'x' symbols, low permeability layers with '+' symbols. The variation in average intensities between different layers is smaller than the variation in intensity along the length of a layer (figure 10) at fixed concentration.

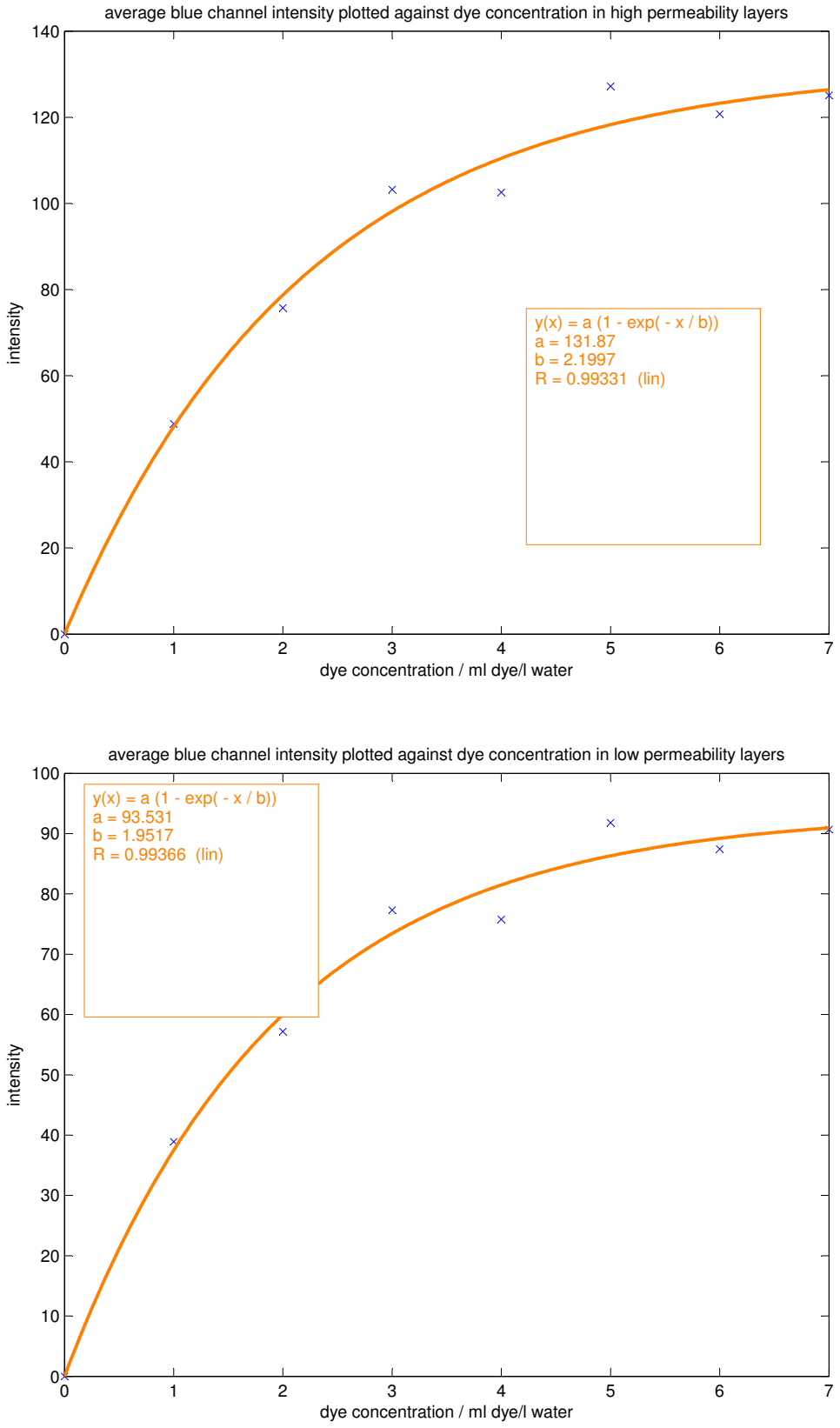

Figure 13: Intensity-concentration plots used to determine concentrations from photographs in experiments with the tank in a horizontal orientation.

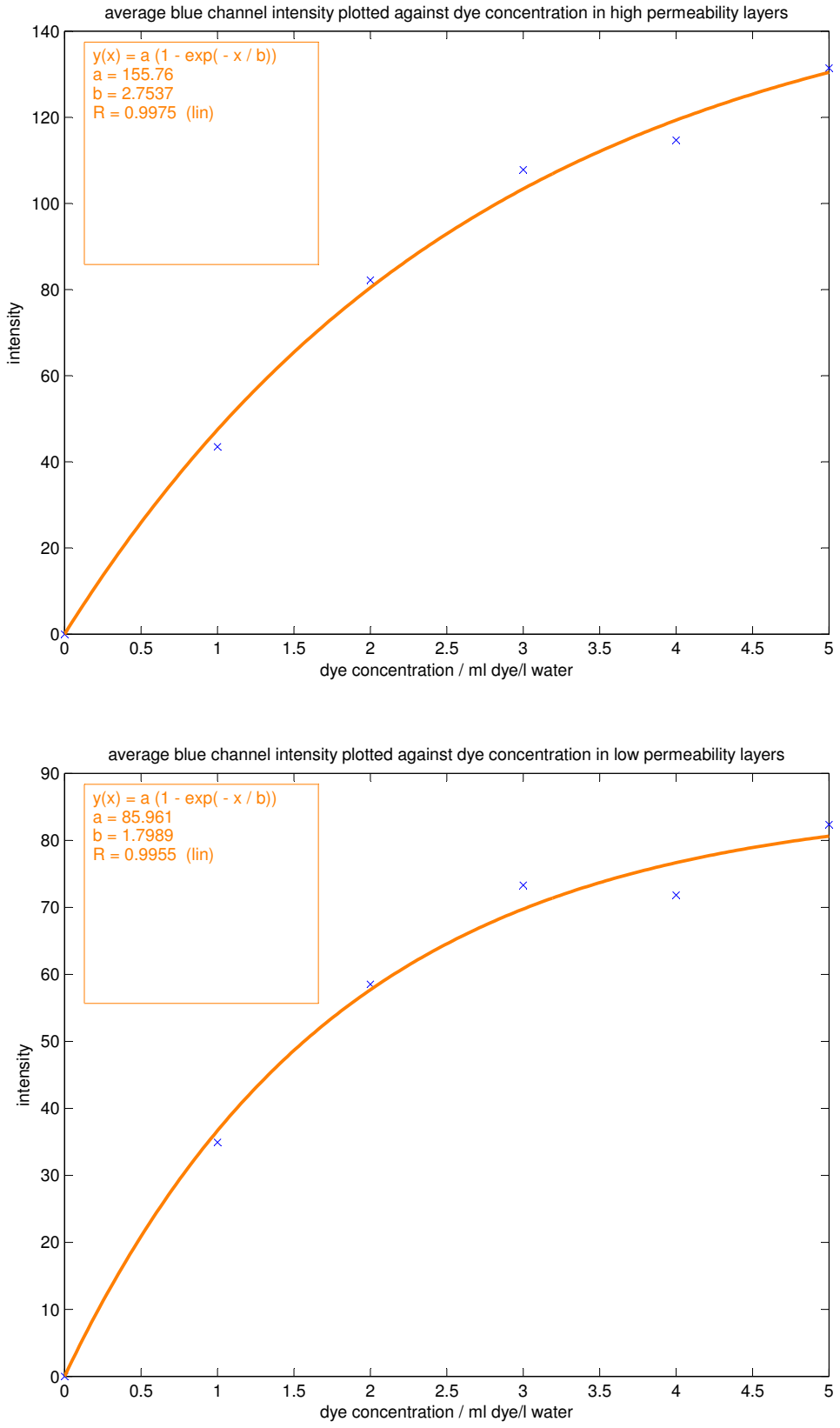

Figure 14: Intensity-concentration plots used to determine concentrations from photographs in experiments with the tank in a vertical orientation.

5 Experimental Results and Analysis

The parameter space for the experimental arrangement was very large and so due to time constraints only those parameters that could be easily altered were varied. These were the fluid properties, the orientation of the tank, and the input flux.

Experiments were first carried out injecting dyed water into a water saturated tank, with the tank orientated horizontally to investigate the flow behaviour without the effects of density or viscosity differences. Subsequent experiments injected water into glycerin in a horizontal tank with the intention of investigating the flow behaviour with a viscosity difference but not a density difference. Finally saline solutions of varying density were injected into glycerin with the tank vertical to investigate the effects with both a viscosity and density difference.

Though the properties of water and glycerin are different to those of supercritical CO_2 and brine, both the real world and experimental systems involve the injection of less viscous, less dense fluid into an ambient fluid that is denser and more viscous. In both cases the two fluids are miscible.

5.1 Analysis of Raw Data

Concentration maps were produced from the raw images using the calibrations in figures 13 and 14. A Matlab script (§D.2) was produced that divided the image into separate layers and calculated concentrations from blue RGB intensity following subtraction from a reference image. A smoothing convolution was also applied to average intensities over several pores and beads to remove bead speckle. Figure 15 shows the effect of transforming a raw image into a concentration map.

The positions of the interfaces in each layer were measured for both the water-water and horizontal water-glycerin experiments. In practice the interface is not abrupt but gradual, and spread out during the experiments. The interface position was therefore measured as the point at which the blue channel intensity, averaged across the width of the layer, crossed a certain threshold value (figure 16). Initially this threshold was chosen to as the intensity equal to half the input dye concentration, as this should correspond to the position of the abrupt interface assumed in theory.

This spreading of the interface is due to hydrodynamic dispersion, caused principally by variations in local velocity at the pore scale due to the complex microstructure of the medium [Bear, 1972].

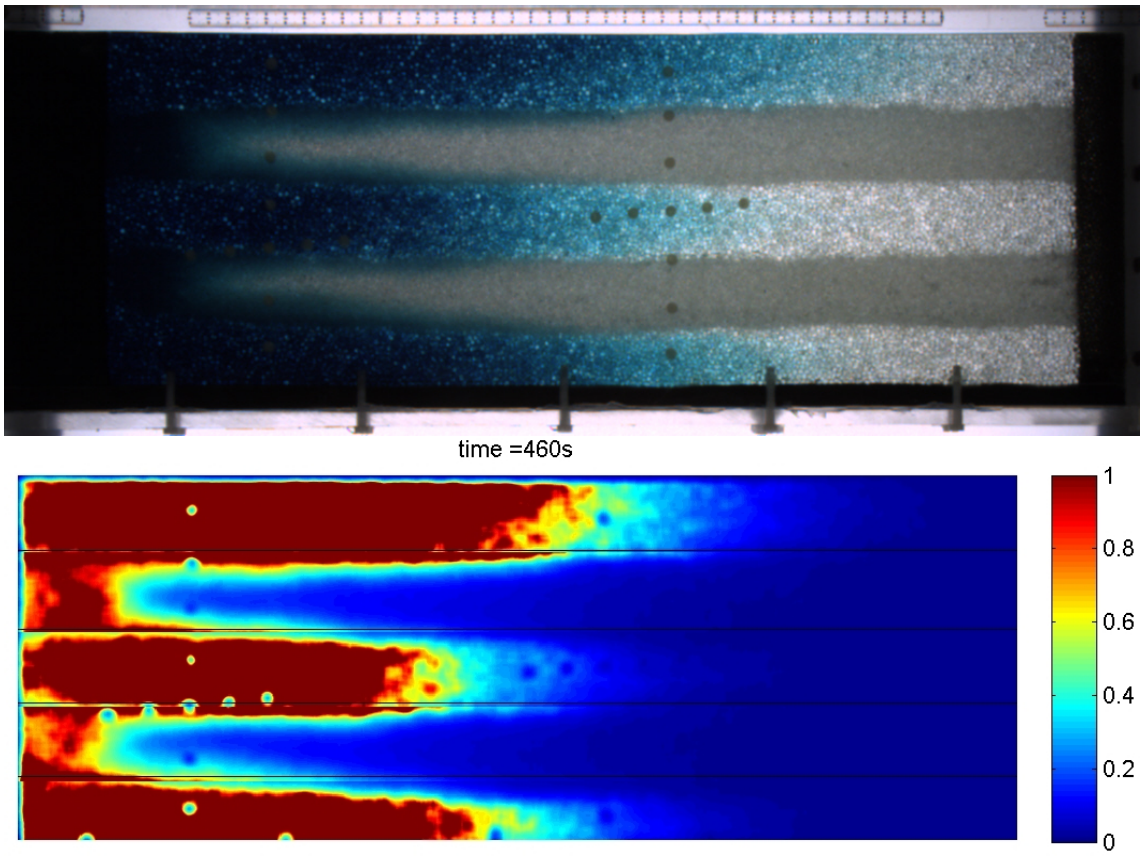

Figure 15: Raw image and corresponding concentration map from a water-water experiment. Black lines mark the edges of the layers as defined for image processing. The large dots on both the raw and processed images are where holes in the tank used in a previous study have been plugged. Some errors arise near the edges of layers as the image is split along straight lines whilst the bead layers in experiments were not perfectly straight. Times given on concentration maps are from beginning of experiment, a short time before fluid enters the porous medium.

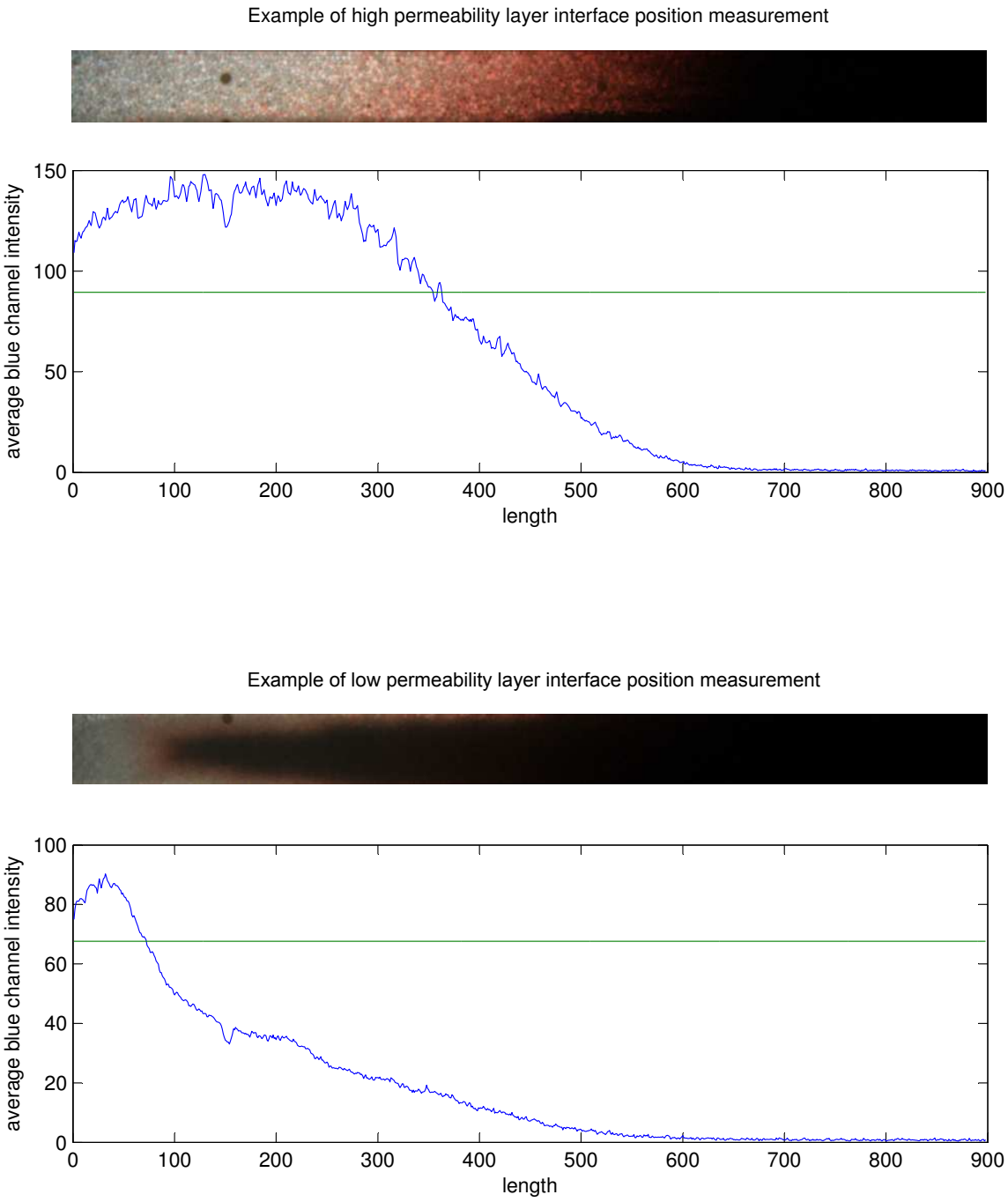

Figure 16: Cropped images of individual high and low permeability layers from the same photograph, following subtraction from a reference image (hence inverted colours). Each is displayed with a layer width averaged intensity profile (blue line) and the threshold intensity (green line). The interface is defined by the last point at which the averaged intensity falls below the threshold.

5.2 Water-Water Experiments

Three experiments were carried out with the tank in a horizontal orientation and water comprising both the injected and ambient fluids. The interface was stabilised under gravity before the start of each experiment as described in §4.1. The injected water had a density of 1.0084 ± 0.0005 gcm^{-3} (errors due to uncertainties in the masses of salt and water measured).

The mass flux varied by altering the rotation rate of the peristaltic pump. Rotation rates of 40, 20 and 10 RPM were used corresponding to mass fluxes of 0.4266, 0.2115 and 0.1037 gs^{-1}. Equation 16 was used to convert these the measured mass fluxes to pressure gradients. These were 53.61, 28.58 and 13.03 Pam^{-1} respectively.

The evolution of the flow with time was similar for all three experiments, with the main difference being the speed of progress of injected fluid along the tank. Concentration maps with time for one of the experiments are shown in figure 17.

5.2.1 Observations and Measured Velocities

The positions of the interface were plotted against time for each layer, the velocity in each layer is given by the slope of the graph. Interface velocities were only measured from the early, linear parts of the curves as later the measured interface positions are dominated by crossflow between the layers, and so cannot be compared to the 1D theory.

The average measured interface velocities are given in Table 2.

Mass Flux / gs^{-1}	High k Velocity / cms^{-1}	Low k Velocity / cms^{-1}
0.4266	0.0779 ± 0.0110	0.0189 ± 0.0013
0.2115	0.0374 ± 0.0062	0.0129 ± 0.0018
0.1037	0.0146 ± 0.0030	0.0024 ± 0.0018

Table 2: Errors given are the standard deviation of the velocities measured from individual layers, errors in mass flux are negligible.

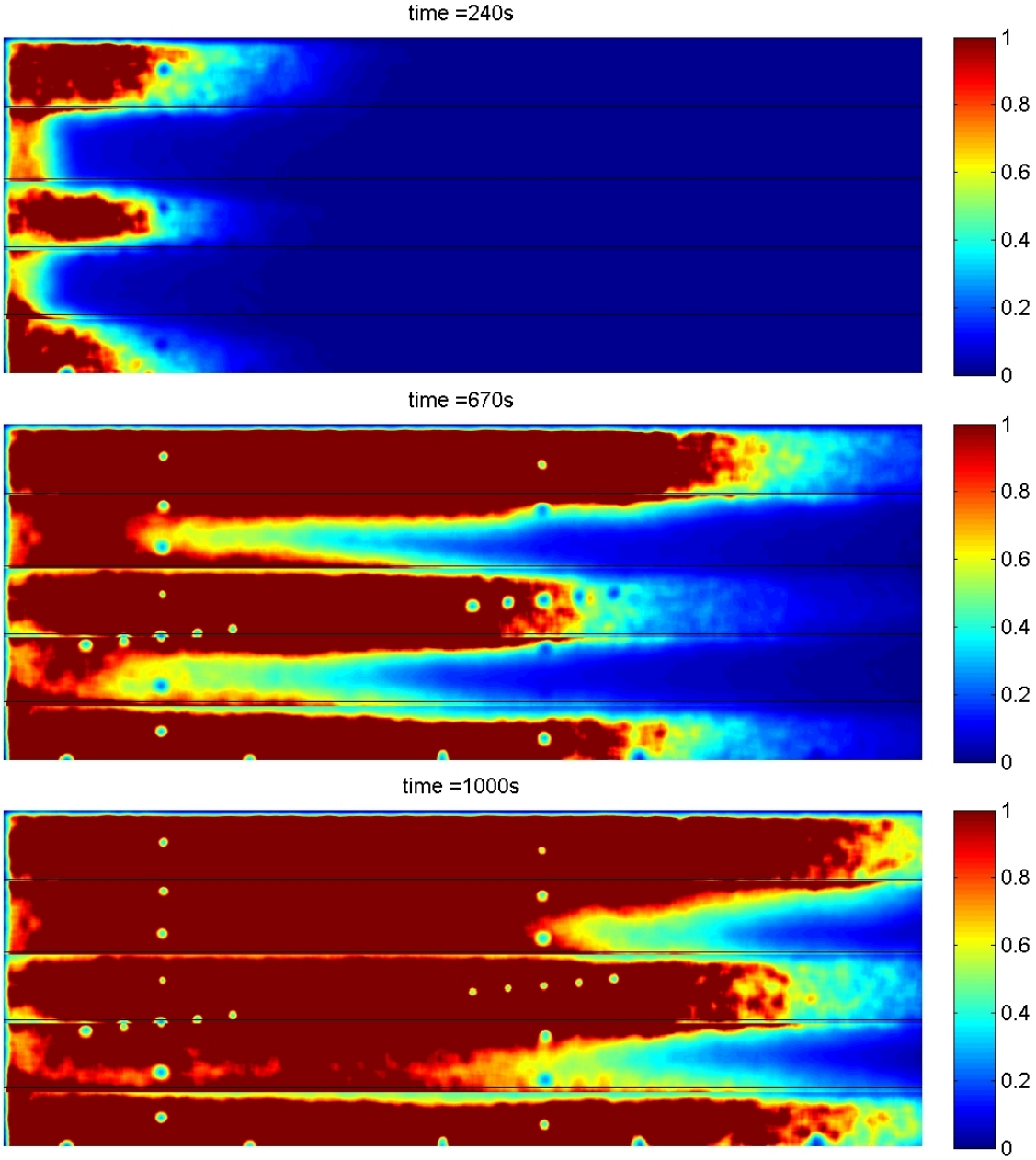

Figure 17: Development of flow following water injection beginning at time = 70 s, at a mass flux of 0.4266 gs^{-1}. There is considerable spreading of the interfaces along each layer, as well as some spreading from the high permeability layers into the low. Towards the end of the experiment, interface progress along the low permeability layers is completely dominated by inflow from the layers either side of them.

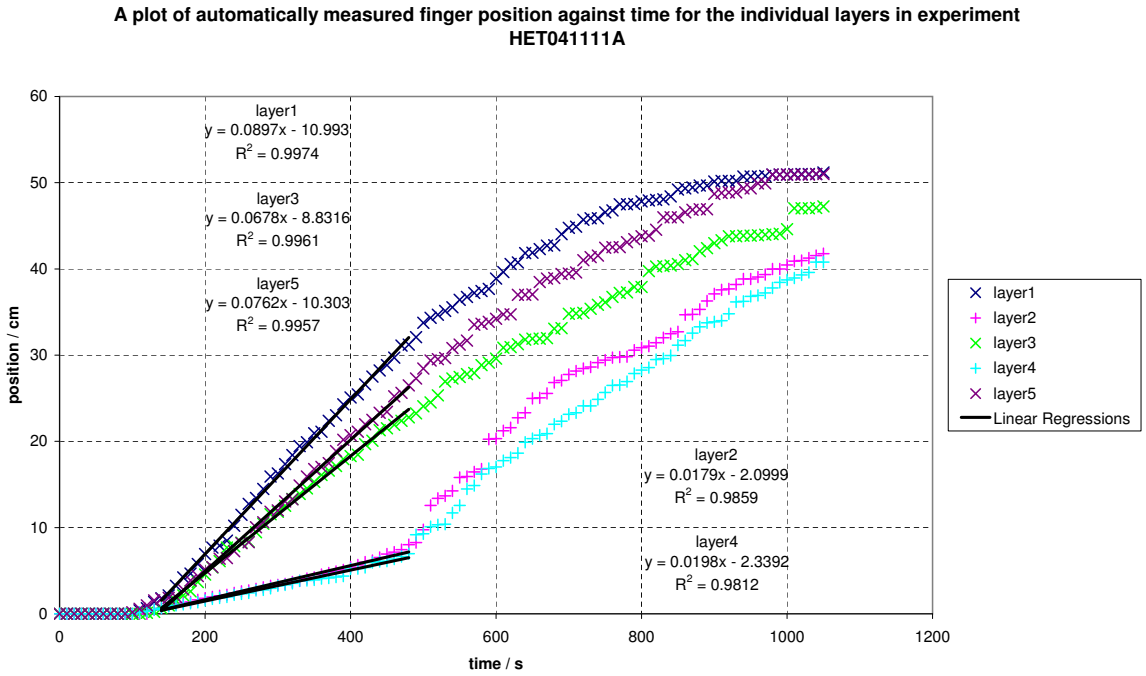

Figure 18: Plot of interface position against time for each individual layer when a mass flux of 0.4266 gs^{-1} is supplied. 3 mm bead layers are marked with 'x' symbols, 1 mm bead layers with '+' symbols. After about 500 s dispersive crossflow from the high permeability layer to the low begins to dominate flow along the low permeability layers, marked by a sudden increase in velocity. The low permeability layer interface velocity then follows that of the high permeability layers.

5.2.2 Comparison to Theory

Theoretical interface velocities were derived from equation 17 using the parameters listed in table 1. These are compared to the measured velocities in figure 19.

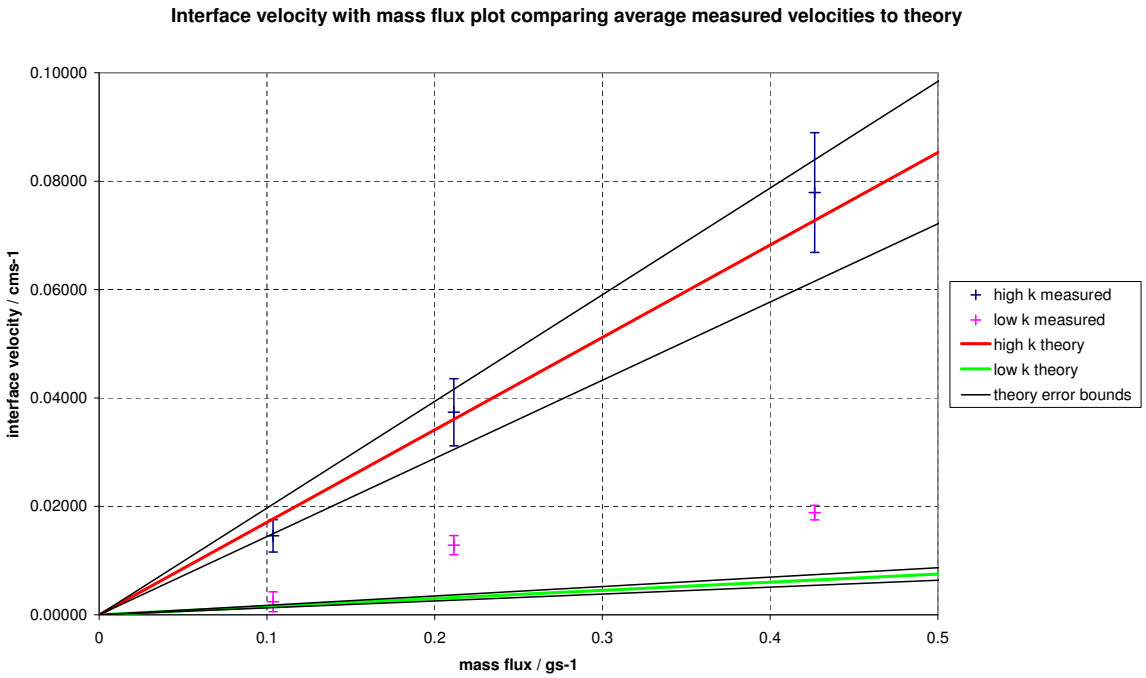

Figure 19: Comparison of measured speeds to theory. Errors in the theory lines are derived from the values listed in table 1 and the error in the density of injected fluid. The velocities measured in the high permeability layers agree well with theory but the velocities measured in the low permeability layer do not agree within error.

The only errors unaccounted for were those in the permeabilities and porosities measured in Strandkvist et al. as no error bounds were given. To attempt to gauge whether the discrepancy in the theoretical and measured low permeability velocities could be accounted for by errors in these values, two other methods of deriving the porosities and permeabilities were used. The results of these calculations are displayed in figure 20, with the values used displayed in table 3.

None of the porosities and permeabilities used agree with the measured low permeability velocities, and so it is unlikely that the source of the discrepancy is due to errors in these values.

Instead it is suggested that unexpectedly high velocities arise from dispersive flow from the 3 mm bead layers into the 1 mm bead layers, before this crossflow begins to dominate.

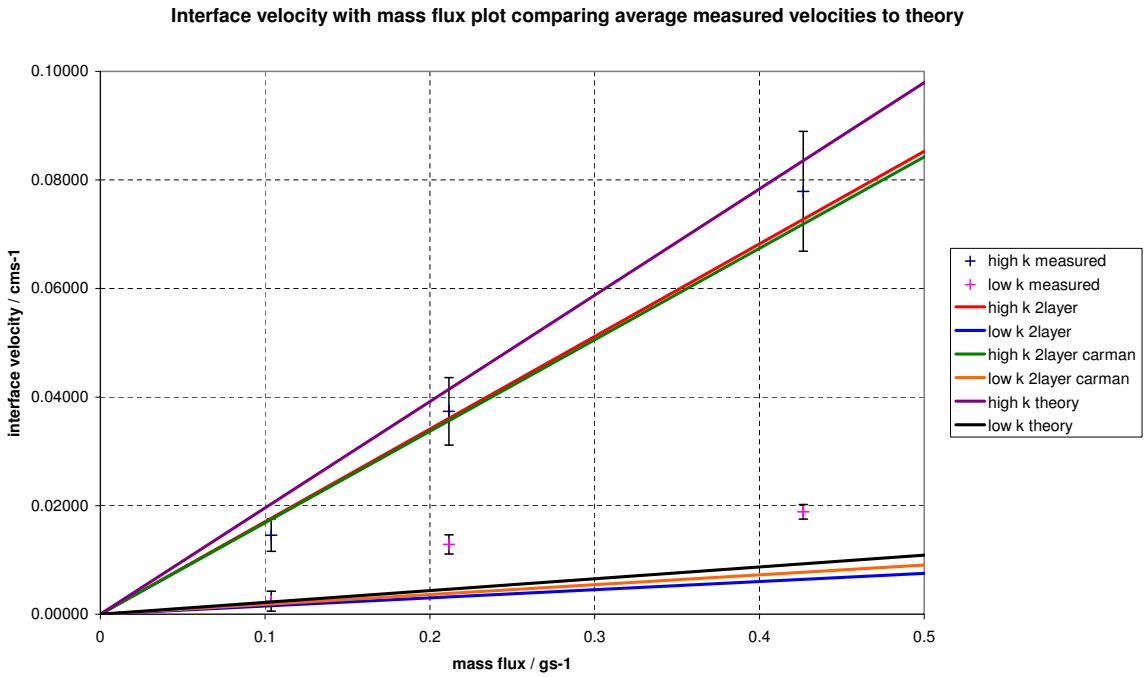

Figure 20: Comparison of measured speeds to theory, using various permeabilities and porosities. The 'high k 2layer' and 'low k 2layer' lines are those measured in Strandkvist et al, the same as those used in figure 19. The 'high k 2layer carman' and 'low k 2layer carman' lines use the porosities measured in Strandkvist et al, with permeabilities calcualted using the Carman-Kozeny model. The 'high k theory' and 'low k theory' lines are calculated using a theoretical porosity for random packed spheres, with permeabilities from Carman-Kozeny.

	2layer Carman	Theory
3 mm bead porosity	0.44	0.375
1 mm bead porosity	0.4	0.375
3 mm bead permeability	1.36×10^{-4}	6.75×10^{-5}
1 mm bead permeability	1.20×10^{-5}	7.50×10^{-6}

Table 3: Porosities and permeabilities used for calculations in figure 20

5.3 Horizontal Glycerin-Water Experiments

A further three experiments were conducted with the tank flooded with glycerin and in a horizontal orientation, with pure water (of density 0.9982 gcm^{-3} [Weast, 1985]) injected at different pump rates. Pure glycerin was too viscous for use in the experiments, causing high pressures and leaking in the tank and leading to excessively long tank flooding times. Instead, a mixture of 90 wt% glycerin and 10 wt% water was used. The kinematic viscosity of the glycerin mixture was measured using a U-tube viscometer, and converted to dynamic viscosity using a density of 1.235 gcm^{-3} [G.P.A., 1963] (see table 4).

Attempts were again made to stabilise the interface under gravity, using the density difference between water and the glycerin mixture. However, viscous fingering of the injected fluid in the sponges adjacent to the injection points rendered this impossible,

Mass Flux / gs^{-1}	Average Dynamic Viscosity / mPas
0.4470	188.1 ± 5.0
0.2126	207.4 ± 1.5
0.1011	191.5 ± 3.2

Table 4: Viscosities were measured from both the input reservoir and tank outputs to ensure complete flooding of the tank. Errors are the standard deviation of 6 individual measurements.

and the injected fluid didn't enter the porous medium at the same time across the width of the tank. As a result, early in the experiments the injected fluid distribution mainly reflected the position of fingers in the sponges.

5.3.1 Observations

The main features of the flow were again similar in all three experiments, with the velocity at which fluid progressed along the tank being the main difference between the experiments. The observations common to all three experiments were:

- Measured concentrations remained low thoughout the experiments (figure 21). This was not an atifact of the image processing to produce concentration maps, as the dye colour is visibly much weaker in the raw images.
- The velocities at which the injected fluid progresses down the high permeability layers is much faster than observed in the water-water experiments.
- The velocities in each of the high permeability layers vary significantly in each experiment.
- There is effectively no progress along the low permeability layers parallel to the length of the tank. Instead they fill almost entirely from adjacent high permeability layers.
- As the injected water progresses along the high permeability layers, branching viscous finger enter the adjacent low permeability layers. However, these retreat into the high permeability layers shortly after the fastest high permeability finger reaches the end of the tank. Later, the low permeability layers begin to fill from the sides again.

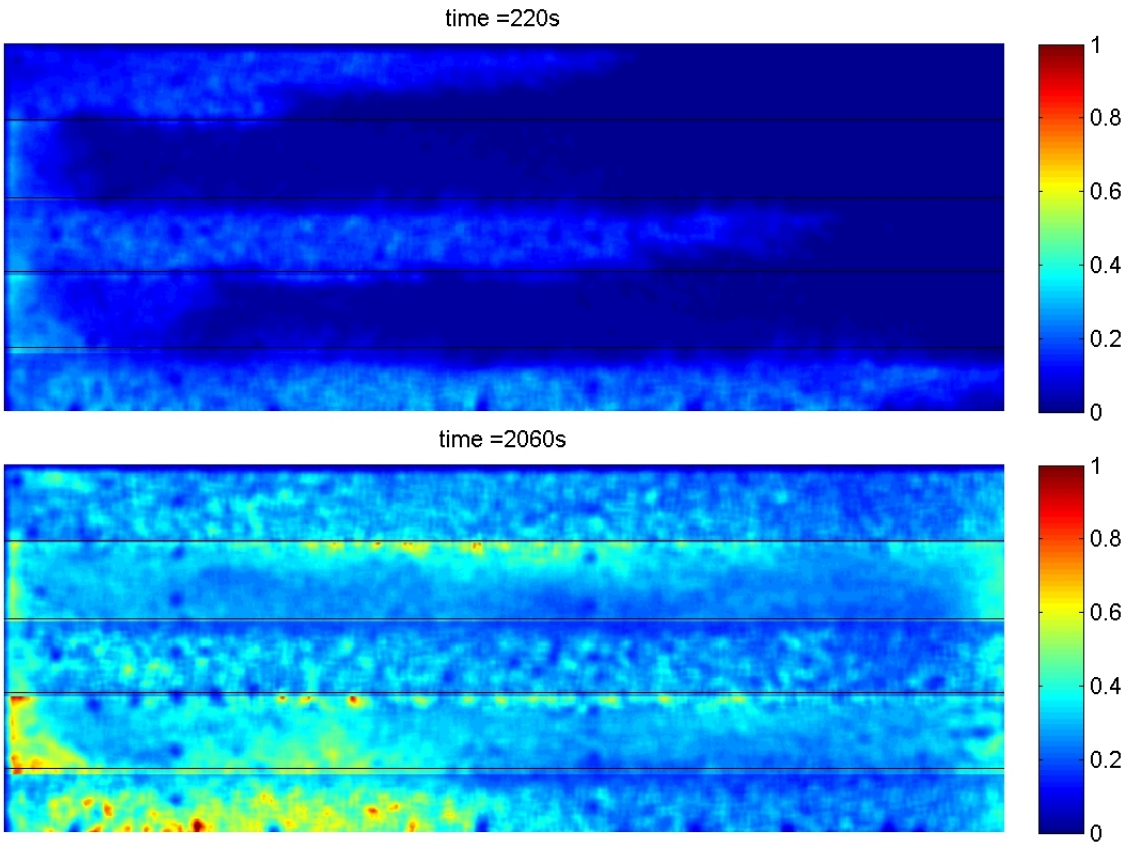

Figure 21: Images taken from a water-glycerin experiment with a mass flux of 0.2126 gs^{-1}. Low concentrations are observed both as the fluid first progresses along the tank (time 220 s), and even after water injection has continued for long enough for the concentrations to reach an apparently steady state (time 2060 s).

5.3.2 Interface Velocities and Override

Due to the low measured concentrations throughout, the width averaged concentrations in each layer never crossed the previous theshold intensity equivalent to half the injected concentration, and so a new threshold intensity was required. This was chosen as half the average concentrations in the high permeability layers at time of breakthrough.

The interface velocities measured from one of the experiments are shown in figure 22. The average measured interface velocities are given in Table 2.

Mass Flux / gs^{-1}	High k Velocity / cms^{-1}	Low k Velocity / cms^{-1}
0.4470	0.3707 ± 0.1802	0.0242 ± 0.0088
0.2126	0.1955 ± 0.1005	0.0066 ± 0.0013
0.1011	0.0985 ± 0.0573	0.0060 ± 0.0013

Table 5: Errors given are the standard deviation of the velocities measured from individual layers. These large errors reflect the large variation in velocity between different layers of the same permeability within these experiments.

Plots of average interface velocity against mass flux show that the measured and

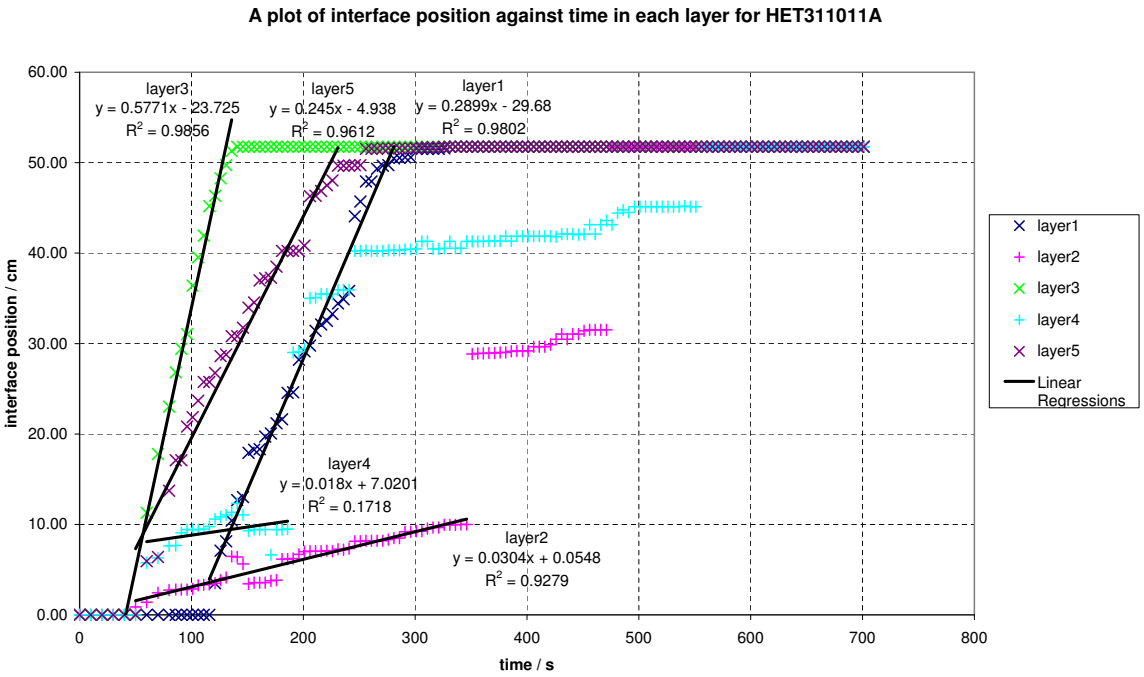

Figure 22: Plot of interface position against time for each individual layer when a mass flux of 0.4470 gs^{-1} is supplied. 3 mm bead layers are marked with 'x' symbols, 1 mm bead layers with '+' symbols. There is a much larger spread in the velocities for a given permeability than seen in figure 18. Note that velocities measured from the low permeability layers are extremely unreliable.

theoretical velocities do not agree within error (figure 23). As demonstrated previously, unnaccounted errors in permeability and porosity are unlikely to be large enough to account for this discrepancy. This suggests that one of the assumptions made is not valid.

Low measured concentrations and faster than predicted interface velocities can be explained by the water overriding (flowing above) the glycerin. Though the depth of the flow could not be observed with the tank in a horizontal orientation, at a constant volume flux the interface velocity can only increase if the flow occupies a smaller cross sectional area. In addition water was observed flowing in a thin layer over a layer of glycerin in the tubes from the tank output nozzles. Due this override, it was not possible to find exact concentrations and the degree of mixing in the tank, due to the implicit depth average taken in the photographs.

Attempts were made to fit the plots in figure 22 with curves of $\xi_i \propto t^{\frac{2}{3}}$, as would be expected if the injected fluid was behaving as a spreading gravity current with a constant flux supplied [Huppert and Woods, 1995]. However, these fits could not improve on the linear regressions in figure 22 and so the flow was treated as occupying a channel of constant thickness, driven primarily by the pressure difference across the tank, with bouyancy forces ignored.

Linear regressions were fitted to the average velocities to obtain the average interface velocity as a function of mass flux (figure 24).

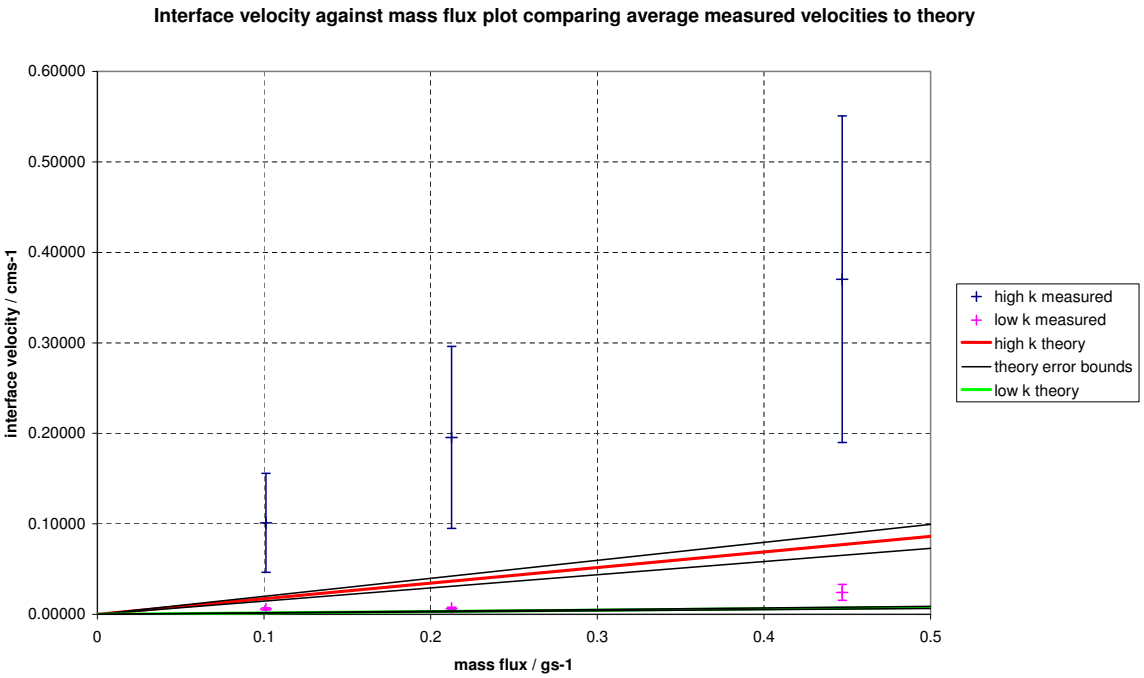

Figure 23: Comparison of average measured speeds to theory. Errors in theory are derived as in figure 19. Both high and low permeability layers do not agree within error.

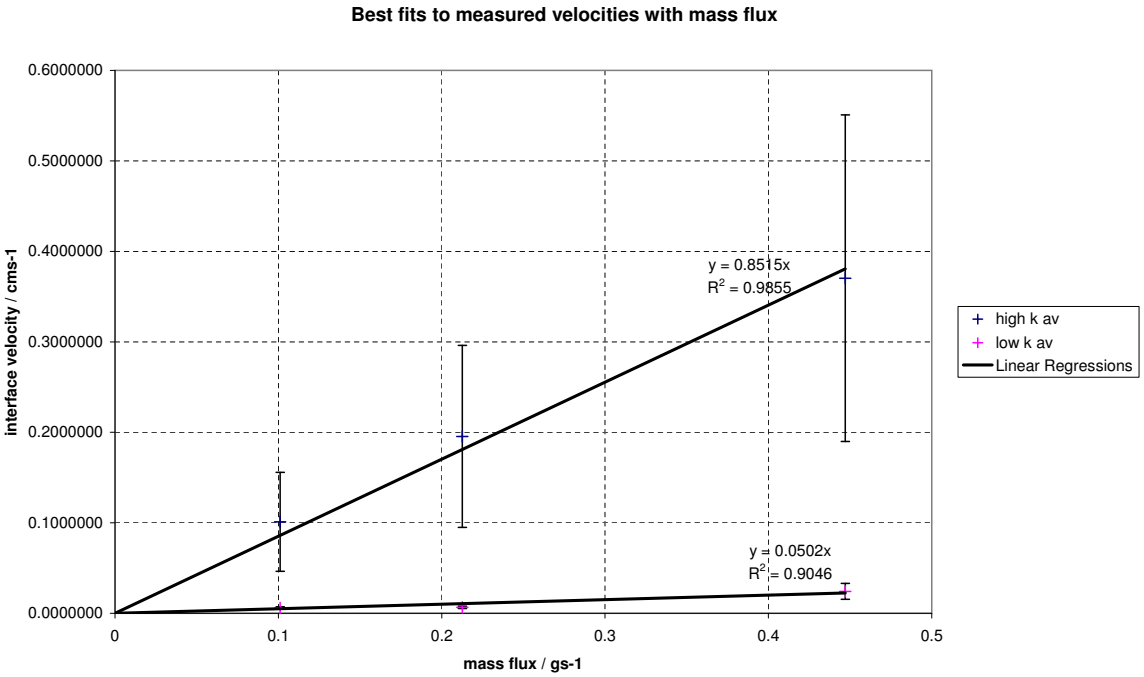

Figure 24: Best fits to plots of average interface velocity against mass flux

The average thickness of the flow can therefore be found using equation 17, replacing the a_i with channel thickness, t multiplied by the widths of each layer, w_i, and solving for t. This gives average channel thicknesses of 2.34 mm and 3.50 mm when calculated from the high permeability and low permeability layer velocities respectively.

5.3.3 Average Driving Pressure Gradients

Unlike the water-water case, average pressure gradients, G, will be dependent on the distribution of fluids in the tank. Knowing the thickness of the water channel allows these average pressure gradients across the tank to be calculated using equation 14. As previously noted the velocities measured from the low permeability layers are likely to be extremely unreliable, and so the channel thickness obtained using the high permeability layer velocities was used.

The tank was treated as having 5 layers of thickness 2.34 mm along which the injected water advances, and 5 layers underneath comprising the remaining thickness of the tank which remain saturated in glycerin. The interface positions measured previously were used to generate plots of G against time for each experiment (see figure 25).

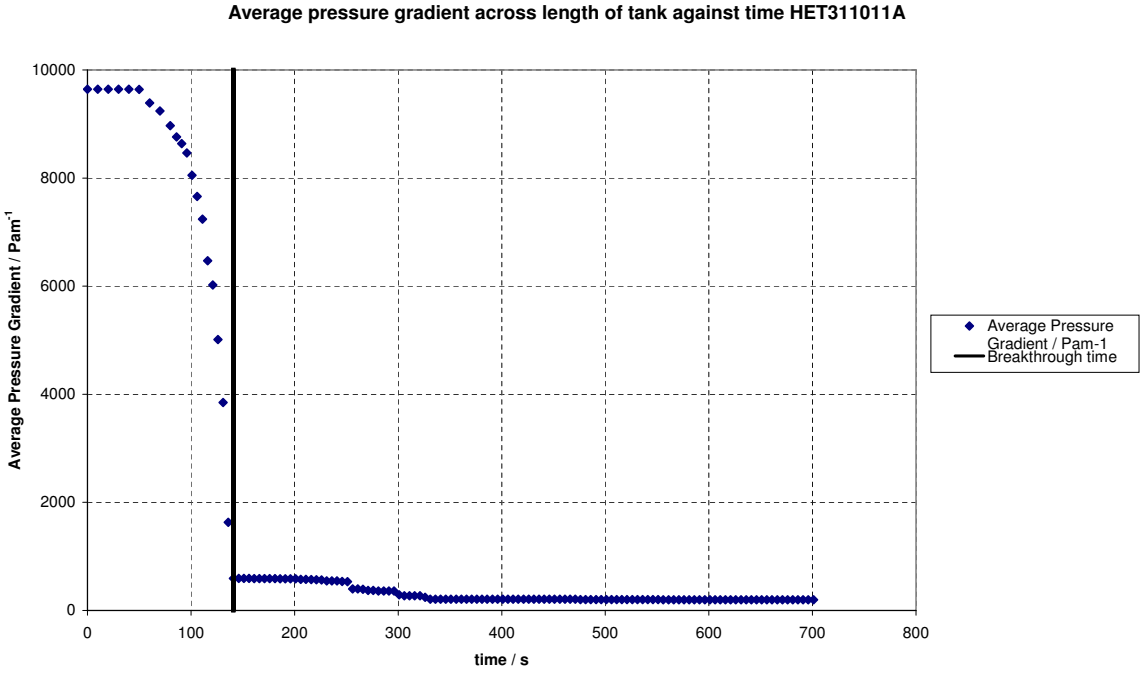

Figure 25: Calculated average pressure gradient, G, with time for a horizontal glycerin-water experiment with a mass flux of 0.4470 gs^{-1}. The breakthrough time marked is when the injected fluid first reaches the end of the tank in one of the layers.

The assumption of a constant flow thickness of 2.34mm is probably not valid after breakthrough but this is unlikely to have a significant effect as the pressure cannot drop below the water filled value of 51.36Pam^{-1}, and so most of the drop in G has already occured by the time the assumption fails. Similar plots were obtained for the other two experiments, summarised in Table 6.

Mass Flux / gs^{-1}	G_s / Pam^{-1}	G_b / Pam^{-1}	G_e / Pam^{-1}
0.4470	9643	593	197
0.2126	5056	636	92
0.1011	2220	288	45

Table 6: Average pressure gradients across the length of the tank at the start (G_s) and end (G_e) of each experiment, and the time of water breakthrough (G_b).

5.3.4 Crossflow Between Layers

Flow between adjacent layers developed in a completely different manner to the water-water experiments. Instead of the steady infill of the low permeability layers due to hydrodynamic dispersion from the more advanced adjacent high permeability layers, growth of viscous fingers into the low permeability layers was followed by retreat of these fingers and stabilisation of the interface. This can be explained by considering the lateral pressure gradients introduced due to different interface positions in adjacent layers, using the theory developed in §3.2.2.

We take the experiment with a mass flux of 0.4470 gs^{-1} as an example. At t = 126 s viscous fingers can be seen to be growing from the middle high permeability layer into the low permeability layers to either side (figure 26).

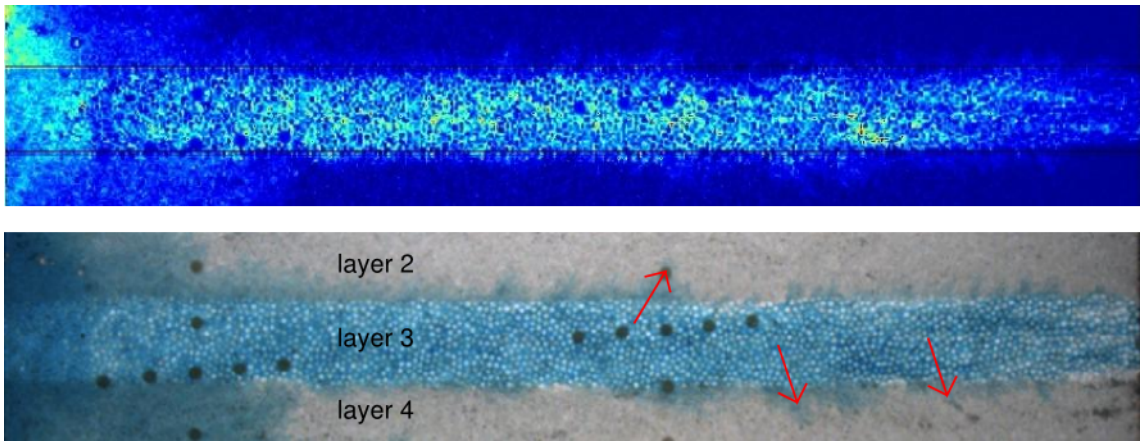

Figure 26: Raw image and Concentration map without smoothing at t = 126 s showing the same section of the tank. Growth of viscous fingers can be seen from the middle high permeability layer (layer 3), into the two adjacent low permeability layers (layers 2 and 4).

A dimensionless plot of interface pressure ($\frac{P}{\Delta P}$) against interface position (ζ) can be produced using the mobility ratio, M, calculated from the measured viscosities, and equation 24. As the pressures gradients are constant, the pressure at all points in a layer can be calculated the interface position is known. The dimensionless pressures, in layers 3 and 4 at t = 126 s are shown in figure 27, calculated using measured dimensionless interface positions of 0.93 and 0.21 respectively.

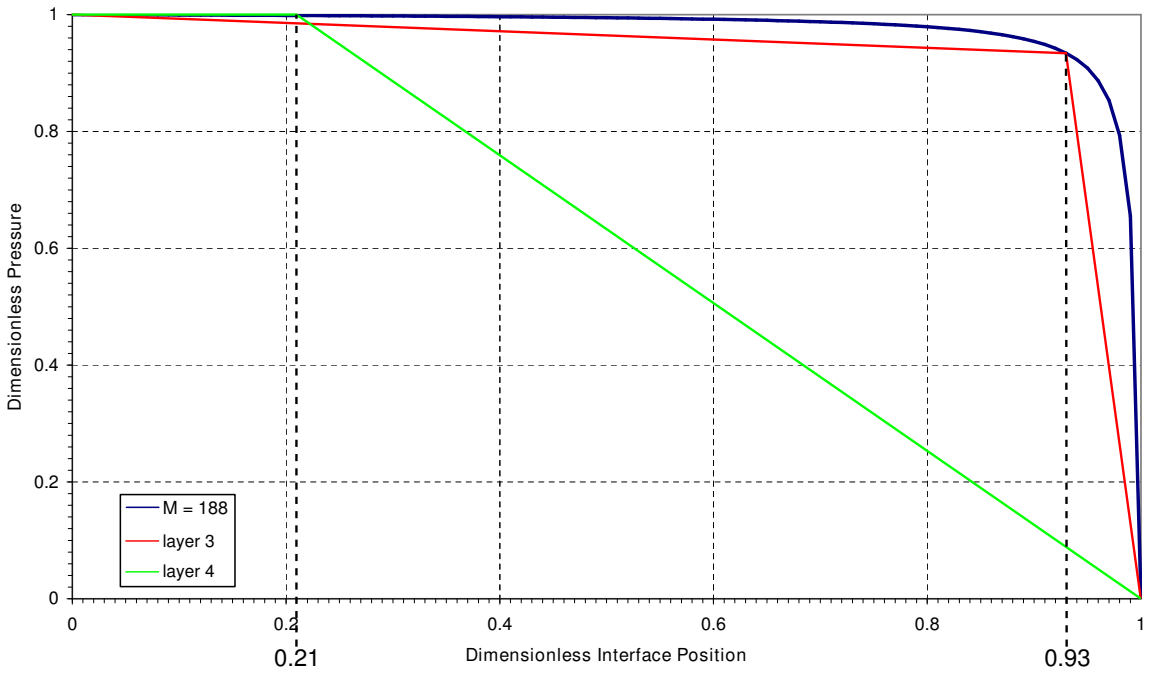

Figure 27: Dimensionless interface pressure with interface position for $M = 188$ is plotted in dark blue. The red line shows the pressures along the length of layer 3, with the green line showing the pressures along the length of layer 4, both at t = 126 s. A pressure difference is created between the layers due to differences in interface position. This pressure difference is largest at $\zeta = 0.93$, the position of the most advanced interface.

The difference in interface position between two adjacent layers therefore drives flow from the layer with the more advanced interface position, into the layer with the less advanced interface position.

By t = 151 s these fingers have largely retreated from the low permeability layers (figure 28), following water breakthrough at about t = 141s.

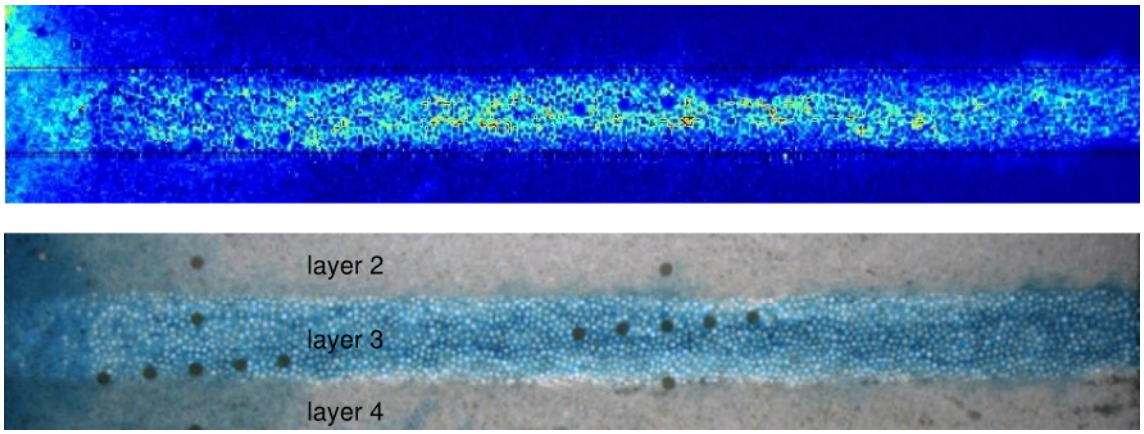

Figure 28: Raw image and Concentration map without smoothing at t = 151 s showing the same section of the tank

---

Again this can be explained by a pressure difference arising from the differences in

interface position. As the interface in the high permeability layer has now reached the end of the tank, the pressure in this layer is now lower than those adjacent to it along the entire length of the tank (figure 29).

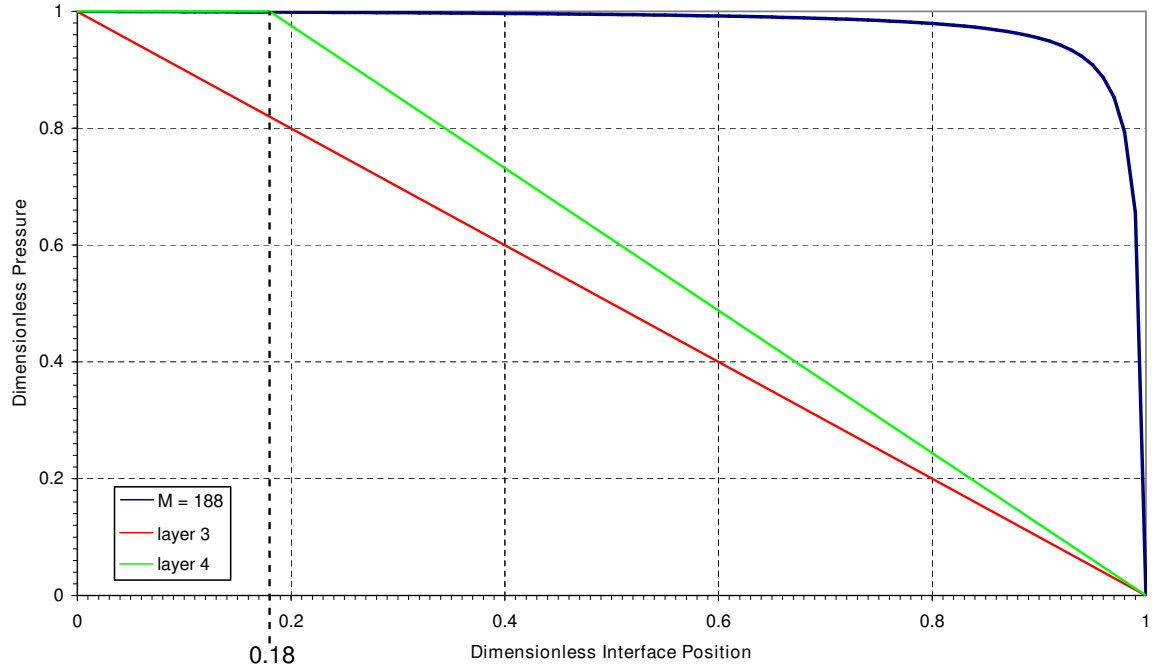

Figure 29: Dimensionless interface pressure with interface position for $M = 188$ is plotted in dark blue. The red line shows the pressures along the length of layer 3, with the green line showing the pressures along the length of layer 4, both at t = 151 s. At this time the pressure gradient acts from the low permeability layers into the high permeability layers and the pressure difference is largest at $\zeta = 0.18$, the position of the interface in the low permeability layer.

The magnitude of this pressure difference between layers will drop with time as the average pressure gradient across the tank drops (figure 25). With this drop in pressure, the water is allowed to spread out into the adjacent layers under gravity. This is believed to be the reason that water again begins to spread from layer 3 into the adjacent low permeability layers after about 300 s.

5.4 Vertical Glycerin-Water Experiments

5 further experiments were carried with the tank intially flooded with a 90% glycerin mixture and the tank in a vertical orientation (width of tank parallel to vertical). Saline solutions ranging from 0 - 26 wt% NaCl were injected at a fixed pump rate of 40 RPM. Mass fluxes vary due to density differences and small variations in volume flux (table 7).

Fluid Density / gcm^{-3}	Mass Flux / gs^{-1}	Dynamic Viscosity / mPas
0.9982	0.4398	184.5 ± 21.9
1.0471	0.4212	193.3 ± 1.6
1.0977	0.4836	199.1 ± 5.0
1.1471	0.4553	191.5 ± 3.5
1.1972	0.5177	204.7 ± 5.3

Table 7: Injected fluid densities, ρ_a [Weast, 1985], mass flux and dynamic viscosity of the 90% glycerin mixture for all verticsl experiments. Glycerin mixture viscosities are averages of 6 readings with errors given by the standard deviation.

Due to the bouyancy of these saline solutions in a glycerin mixture of density 1.235 gcm^{-3}, fluid could not be supplied evenly across the width of the porous medium as it flowed to the top of the sponges from the injection nozzles before reaching the medium.

The tank was therefore modified by removing the high and low permeability sponges at the input end (increasing the length to 57.1 cm) and creating four layers of equal thickness (4.7 cm each), each supplied by an input nozzle. The assumption of equalised pressure at the input end of the tank may no longer be valid, but at least an approximately equal volume flux should be supplied into each layer.

5.4.1 Observations

Two distinct endmember flow regimes were observed:

1. At the highest density contrast ($\rho_a = 0.9982$ gcm^{-3}), injected fluid progresses predominantly along the upper high permeability layer, and more slowly along the lower high permeability layer. The growth of the lower finger stops shortly after the upper finger reaches to the end of the tank and it eventually begins to retreat. The sharp interface at the base of the upper finger then migrates downwards with time as the experiment continues (figure 30).

2. At the lowest density contrast ($\rho_a = 1.1972$ gcm^{-3}), injected fluid breaks-through in both of the high permeability layers. Two stable fingers of water with sharp interfaces to the surrounding glycerin are formed, filling the top of each high permeability layer (figure 31).

At all of the intervening densities the injected fluid reaches the end of the tank in both high permeability layers, as in flow regime 2. However, the concentration in the lower high

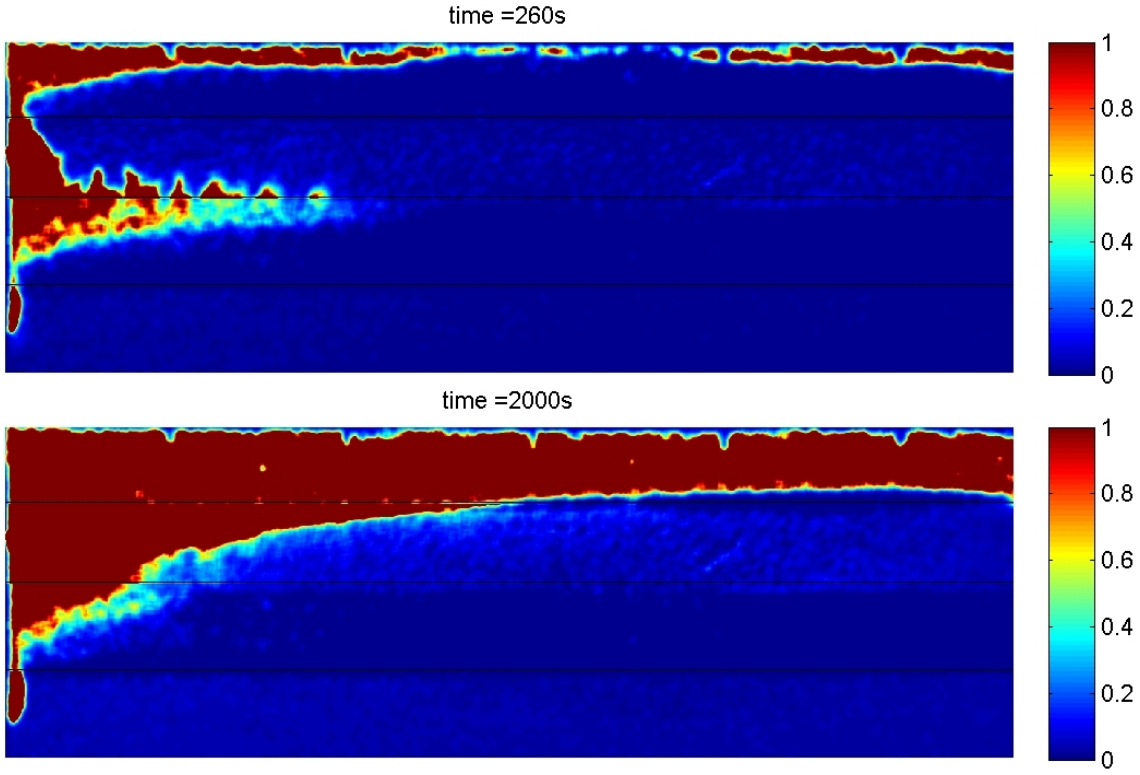

Figure 30: Concentration maps from an experiment where water of density 0.9982 gcm^{-3} is injected into 90% glycerin mixture, showing retreat of the lower finger and flow concentrated along the top of the tank. The low concentration zone in the middle of the top layer of the at time 260 s occurs as compaction of the beads has left a gap between the the beads and the packing sponge, creating a thinner zone of faster fluid flow.

---

permeability layer then began to drop in the experiments with injected densities 1.0471 and 1.0977 gcm^{-3} and flow became concentrated along the top of the tank, as in flow regime 1 (figure 32). With an injected density 1.1471 gcm^{-3}, flow regime 2 was observed, though the uppermost low permeability layer became filled later in the experiment.

In all cases pore scale viscous fingers intrude protrude from the main water fingers as they progress down the tank but then stop growing and retreat to leave a smoother interface. These fingers grow from both the upper and lower surfaces of the flows at all density contrasts. However, the lower interfaces stabilise more rapidly that the upper interfaces.

There is almost no progress along the low permeability layers, with the top low permeability layer appearing to only fill due to flow upwards from the layer below and by downwards motion of the interface at the base of the top high permeability layer.

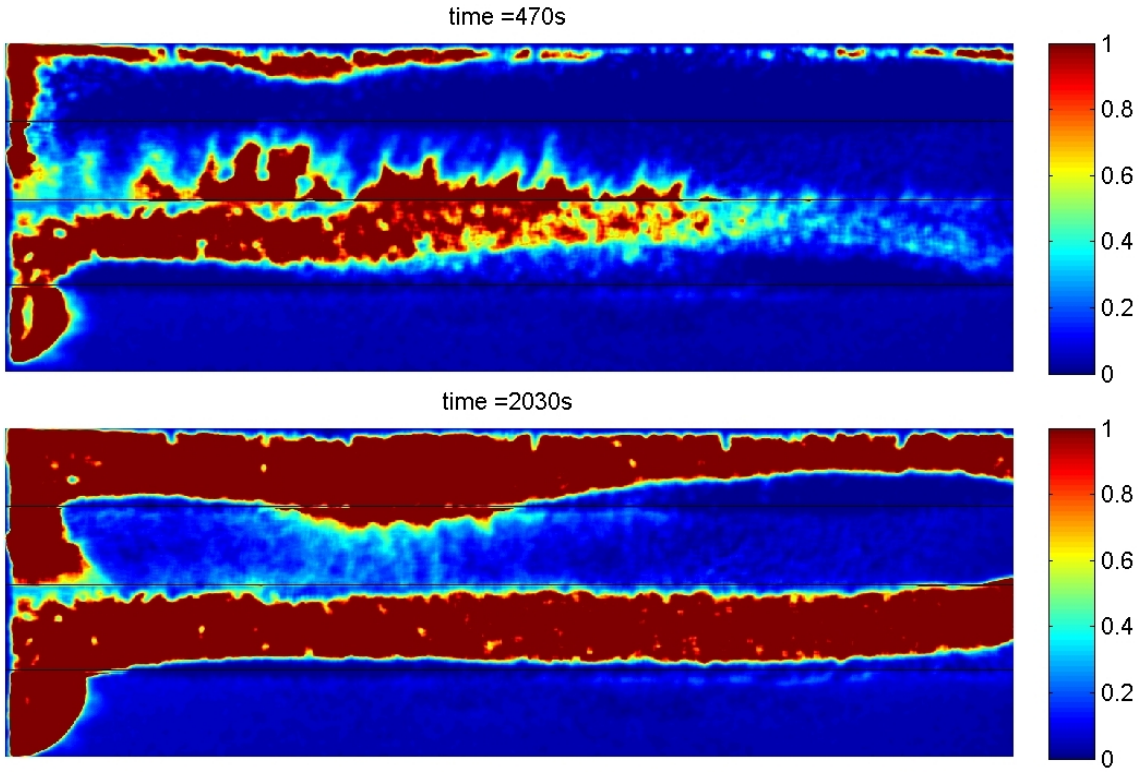

Figure 31: Concentration maps from an experiment where water of density 1.1972 gcm^{-3} is injected into 90% glycerin mixture, showing the formation of two stable fingers.

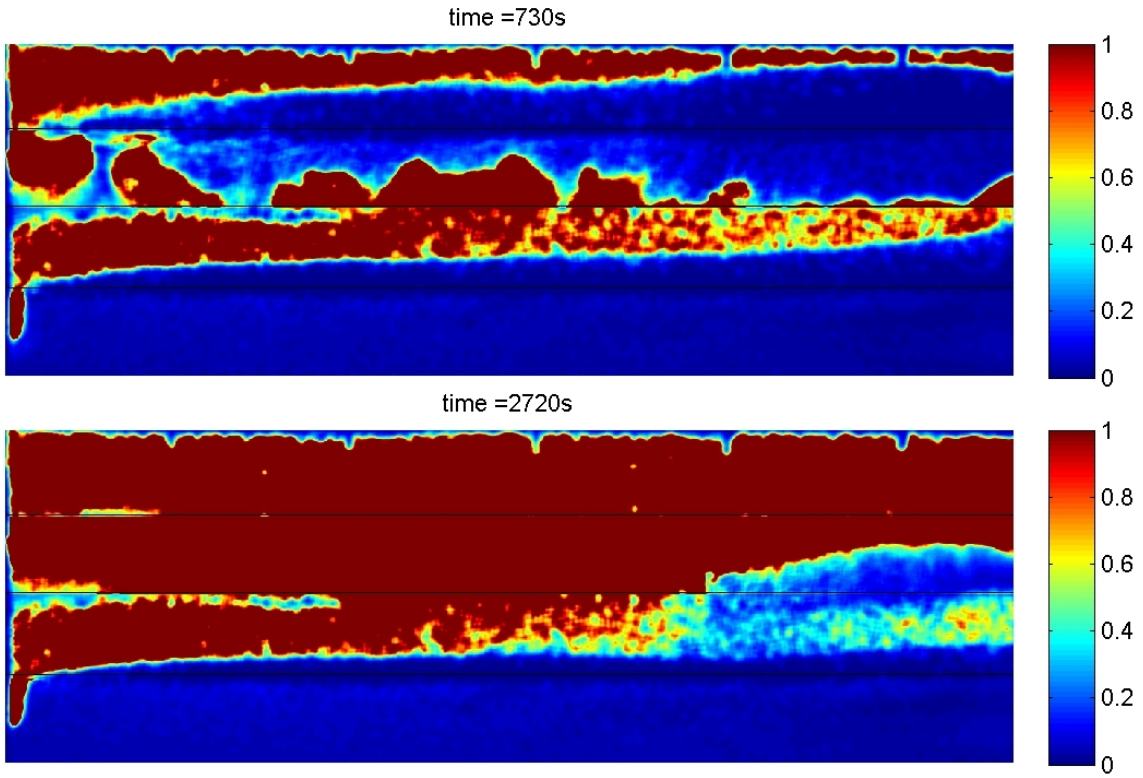

Figure 32: Concentration maps from an experiment where water of density 1.0977 gcm^{-3} is injected into 90% glycerin mixture, showing the change in flow regime.

5.4.2 Average Driving Pressure Gradients

The pressure field in the tank will now depend on both the driving pressure applied across the tank and bouyancy forces acting within the tank. In these experiments the relative magnitudes of these pressures will have important effects on the nature of the flow and so it is important to be able to quantify them.

The use of average interface positions within each layer to calculate G, as in §5.3.3, cannot be applied in these experiments, and so a numerical integration was performed in Matlab, using equation 15, and measuring the interface positions along each row of pixels in the photographs to find the distribution $\zeta(z)$ (§D.4). This method is susceptible to large errors early in the experiments as viscous fingers growing perpendicular to the layers can give apparently higher interface postions. Errors may also arise due to the significant component of vertical flow, which was assumed to be negligible in the theoretical derivation of equation 15, and if there are significant deviations from the assumption of equalised pressure at the end of the tank.

As in §5.3.3, the calculated pressure across the tank drops rapidly until breakthrough, and then drops more slowly (figure 33). Similar plots were observed for the other experiments summarised in table 8.

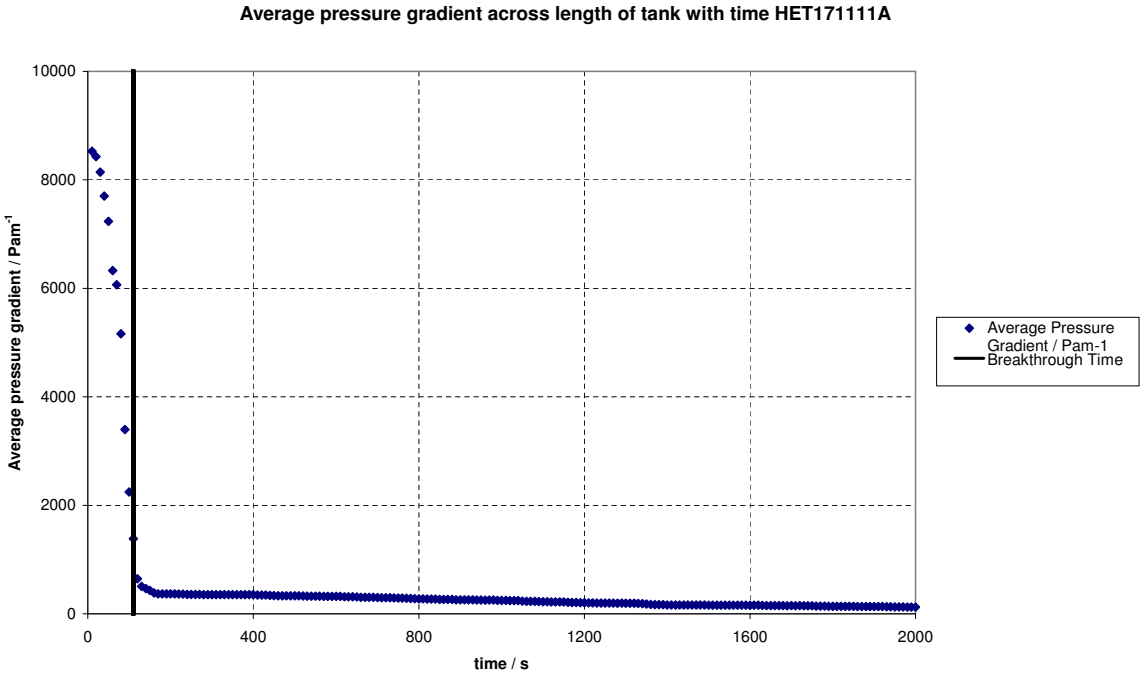

Figure 33: Example plot of average driving pressure gradient, G, against time for a vertical glycerin-water experiment with $\rho_a = 0.9982$ gcm^{-3}. Experiment continues until t = 7380 s but this was omitted for clarity in the early part of the experiment, where pressures change most rapidly.

Injected Density / gcm^{-3}	G_s / Pam^{-1}	G_b / Pam^{-1}	G_e / Pam^{-1}
0.9982	8527	1386	105
1.0471	8008	563	85
1.0977	8895	559	65
1.1471	8380	1301	54
1.1972	8697	1314	78

Table 8: Average pressure gradients across the length of the tank at the start (G_s) and end (G_e) of each experiment, and the time of water breakthrough (G_b). Large differences in breakthrough pressure are due to the rapid changes in pressure around the time of breakthrough and the limited temporal resolution of photos.

5.4.3 Controls on Flow Regime

The large drops in driving pressure are thought to cause the changes in flow regime in experiments at injected fluid densities of 1.0471 and 1.0977 gcm^{-3}, as this will change the relative magnitude of driving and bouyancy forces. The growth and retreat of the lower finger when an injected density of 0.9982 gcm^{-3} is used can also be treated as a change in regime as initially water is forced along both high permeability layers, though water does not breakthrough in the lower layer.

With the change in flow regime, the injected fluid concentrations in the lower high permeability layer (layer 3) are seen to drop. A Matlab script (§D.5) was used to find the fraction of each layer occupied by injected fluid. The change in regime is deemed to occur when this fraction begins to fall in layer 3, as this represents a change from flow concentrated along both of the high permeability layers, to flow concentrated solely along the top of the tank (figure 34).

Injected Density / gcm^{-3}	t_p / s
0.9982	500
1.0471	810
1.0977	2070
1.1471	no change
1.1972	no change

Table 9: Time, t_p, at which fraction of layer 3 occupied by injected fluid peaks, taken to mark the change from flow regime 2 to flow regime 1.

The pressures (calculated in §5.4.2) at which each regime was observed can now be plotted. When plotted as a function of the density contrast between the fluids, it can be seen that regime 2 is favoured by high driving pressure and low density contrasts, and regime 1 is favoured by low driving pressures and high density contrasts (figure 35), as expected.

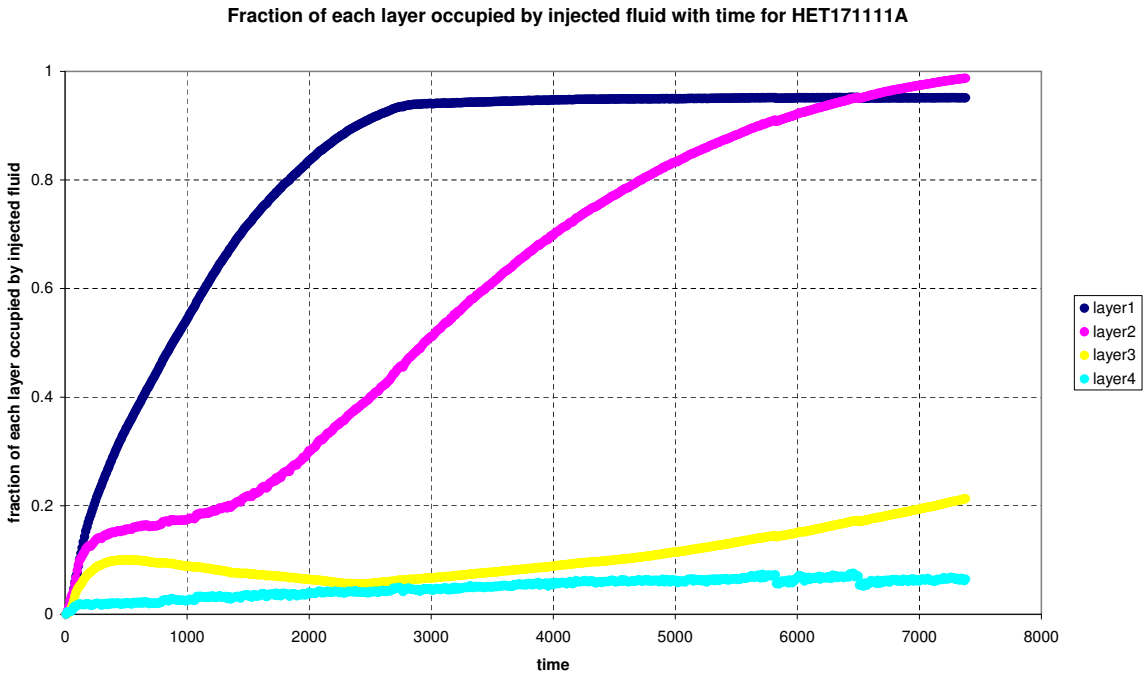

Figure 34: Plot of the fraction of each layer occupied by injected fluid against time for an experiment where the fluid injected has density 0.9982gcm^{-3}. The amount of injected fluid in layer 3 peaks at 500 s, though values are within 5% of this between 350 and 740 s. The later rise in the water-filled fraction of layer 3 is due to filling from above as the stable interface between water and glycerin moves downwards with time.

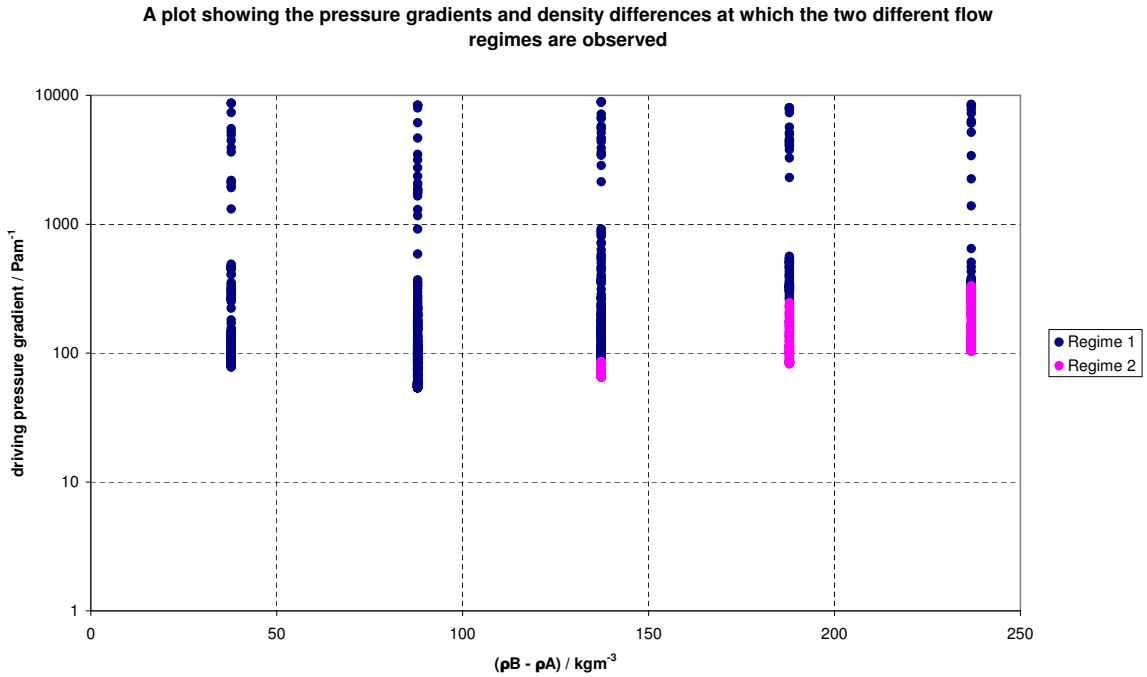

Figure 35: Plot of average driving pressure gradient against density contrast, showing the flow regime observed. Note logarithmic vertical scale.

5.4.4 Lower Finger Retreat

The driving pressure gradients calculated and a simple consideration of the pressure gradients generated by bouyancy forces within the tank can explain the retreat of the lower

finger observed in the highest density contrast experiment. The fraction of injected fluid in the layer should peak when finger retreat begins (figure 34), as no upwards flow into the overlying low permeability layer was observed after the first 400 s.

At 500 s the average driving pressure gradient is calculated at 330 Pam^{-1}. This must be balanced by another force to prevent the continued flow of water along the layer. This finger can be shown to be gravitationally unstable by considering the vertical pressure gradients at various points along its length. The water is treated as a wedge with a sharp interface to the surrounding glycerin (figure 37). The vertical pressure gradient, $\frac{\partial P}{\partial z} = \rho g$, and so will be greater in the glycerin mixture than the water. It is assumed that the pressure at the top of the layer is equal along the length of the wedge.

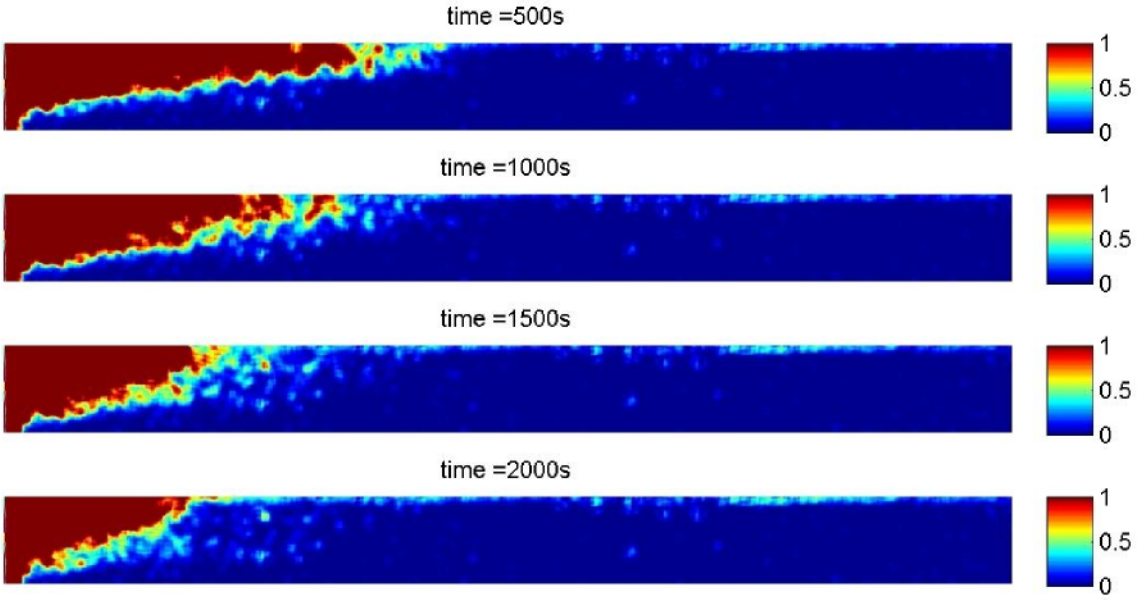

Figure 36: Retreat of the water intruding the lower high permebility layer after 500 s.

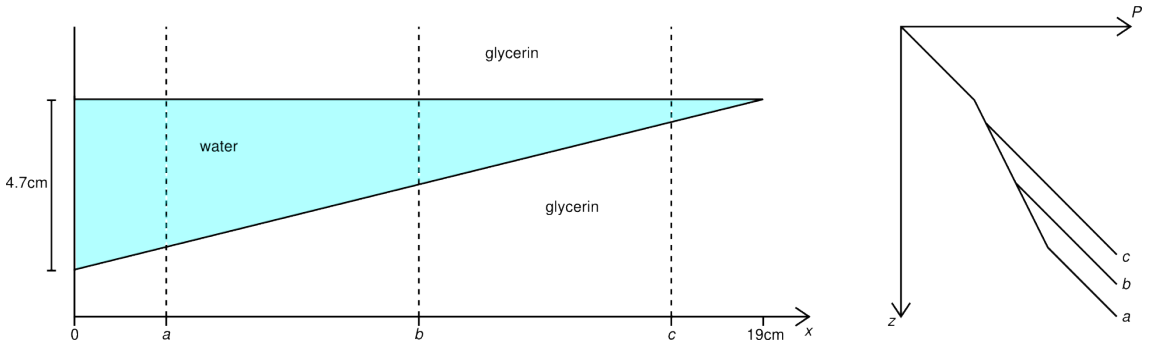

Figure 37: Schematic diagram of the water intruding the lower high permeability layer and the vertical pressure changes at $x = a$, $x = b$ and $x = c$. The layer is 4.7 cm thick, and the nose of the current is at 19 cm. Vertical pressure gradients caused by differences in interface position are ignored.

These vertical pressure gradients can be seen to create horizontal pressure gradients

along the length of the wedge - at a given depth within the wedge, $P_c > P_b > P_a$. The difference in pressure gradient between glycerin and water is $g(\rho_B - \rho_A)$, which for a 90% glycerin mixture and water is 2370 Pam^{-1}. The pressure difference at a depth halfway through the wedge between $x = 19$ cm and $x = 0$ cm is 55.7 Pa, giving a horizontal pressure gradient of 293 Pam^{-1} acting against the driving pressure. This is a crude approximation but demonstrates that the pressure gradients driven by bouyancy forces can be large enough to counteract the driving pressure. This pressure gradient due to bouyancy will in fact be larger due to a similar sloping interface in the top high permeability layer, which was ignored for this calculation.

As the experiment continues, the driving pressure falls further, reaching 123 Pam^{-1} by 2000 s. The bouyancy forces are therefore able drive the retreat of the water in this layer.

6 Discussion

6.1 1D Analytical Model

A 1D analytical model adequately predicted the flow velocity of fluids in the high permeability layers of the water-water experiments. However, departure from theory in the low permeability layers suggests that flow between layers due to hydrodynamic dispersion cannot be ignored in this situation.

The 1D model underestimated the fluid velocities in the horizontal glycerin-water experiments as the assumption of a 2D tank was invalid due to override of the water. However, the flow velocities measured in the high permeabilities are constant, as expected from the model, and show a good fit to flow in a thin channel of constant thickness in the upper quarter of the tank. Flow velocities measured from the low permeability layers were unreliable, but still much lower than expected from the model.

It is suggested that these low velocities, aswell as the large range of velocities observed in the high permeability layers, can be explained by the amplifying effects of the Saffman Taylor instability. As explained in §3.1, any small displacement δx, will amplify due to the viscosity contrast. Therefore the permeability differences between layers may channel flow down the high permeability layers, and small heterogeneities between layers of the same permeability may lead to substantial differences in measured flow velocity.

The growth and withdrawal of pore-scale viscous fingers perpendicular to layers can be explained qualitatively by considering the lateral pressure gradients introduced due to variations in interface position between adjacent layers. The magnitude of the pressure gradients generated could be found by measuring the velocity of advance and retreat of these fingers with time, and calculating pressure gradients from this. However, the relatively low temporal resolution (10s between photos in most experiments) and rapid changes in average pressure gradient across the tank precluded these measurements in this project. Further experiments are suggested, using a constant pressure gradient, and a shorter interval between images, to measure the growth and retreat of these layers for comparison with the 1D theory.

6.2 Crossflow in EOR

The lateral pressure gradients generated by differences in interface position in adjacent layers may affect mixing between CO_2 and the ambient brines in EOR. The size of these pressure gradients will depend on the mobility ratio (figure 6). Though the mobility ratios used in these experiments are much higher ($M \approx 200$), for the range of mobility ratios relevant to the pressures at Salt Creek ($M \approx 10$ - 50 using viscosities from [Burke, 2011]), there will still be appreciable pressure gradients perpendicular to the layers (figure 38). Even at the lower end of this range, with $M = 10$, the maximum pressure difference

generated by this mechanism will be 0.52 ΔP, where a layer with dimensionless interface position, $\zeta_i = 0.76$ is adjacent to either an impermeable layer, or one in which CO_2 has broken through.

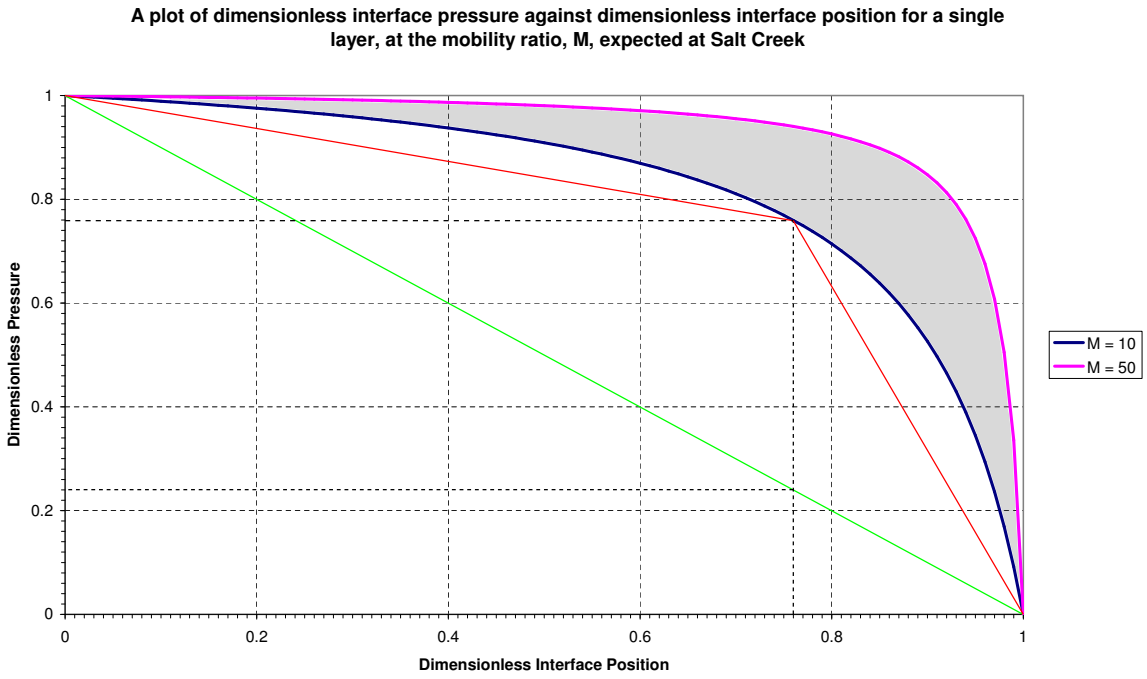

Figure 38: Blue and Pink lines show the variation of dimensionless interface pressure with position across typical mobility ratios for CO_2 sequestration. Red and green lines show the pressures in adjacent layers that will generate the largest cross-layer pressure gradients, with $\zeta_i = 0.76$ in the red layer, and $\zeta_i = 0$ or 1 in the green layer.

In practice the pressure gradients encountered in a real reservoir may be smaller than this if the assumption of no flow perpendicular to the layers is invalid.

Before breakthrough they will act to promote mixing as the most advanced fingers of intruding CO_2 will be at a higher pressure than the adjacent layers. This will drive the growth of viscous fingers into the adjacent layers, greatly increasing the surface area of the interface, and so dissolution between CO_2 and brine. This may be able to explain the large degree of dissolution of CO_2 observed in brines at the Salt Creek injection experiment. However, following breakthrough, the pressures in the most advanced CO_2 fingers will drop such that they are at a lower pressure than adjacent layers. This will counteract the growth of viscous fingers and may force them to retreat, reducing the area of contact between the two fluids.

6.3 Flow Regimes and Mixing

The two different flow regimes observed in §5.4.1 may have an effect on the amount of mixing between CO_2 and brine in a reservoir, for two main reasons. Firsty, the permeability controlled regime has a greater interfacial area between the two fluids due to the

formation of more than one stable water layer. Secondly, stronger pore scale fingering is observed from the top surfaces of the lower water layers than the bottom surfaces of either layer. These upper surface fingers also take longer to retreat (e.g. figure 31).

The stronger fingering from the upper interfaces can be explained by considering equation 3. A small displacement, δx, upwards from a layer will be amplified both by the viscosity contrast and the density contrast (as $\rho_A < \rho_B$ and g is negative for an upwards displacement). For downwards displacements of the interface from the lower layer, density contrasts will act to reduce the change in pressure δp, and suppress fingering. The retreat of fingers from the upper surfaces takes a longer time for similar reasons, as pressure gradients caused by differences in interface position must counteract the bouyancy of the fingers.

Flow regime 1 was found to be favoured by high bouyancy forces relative to driving pressures, and the crossflow between layers is dominated by gravity. Flow regime 2 was found to be favoured by high driving pressures relative to bouyancy forces, and crossflow between layers is controlled by pressure gradients arising due to differences in interface position between layers and the viscosity contrast between the fluids. The transitions between such viscous and gravity controlled flow regimes have been found previously to be related to the gravity number, N_{gv}, so that

$$N_{gv}\frac{M}{1+M} = c \tag{25}$$

at the transition between flow regimes, where M is the mobility ratio and c is constant [Cinar et al., 2006]. The gravity number is defined

$$N_{gv} = \frac{\Delta\rho g L k_{av}}{H u \mu_B}, \tag{26}$$

where $\Delta\rho$ is the density difference, L and H and the width and height of the medium, k_{av} is the average vertical permeability, u is the total velocity and μ_B is the viscosity of the displaced fluid. Making the substitution $M = \frac{\mu_B}{\mu_A}$, equation 25 simplifies to

$$\frac{L}{H}(\Delta\rho g)\frac{k_{av}}{u(\mu_A+\mu_B)} = c. \tag{27}$$

Applying Darcy's law it can be seen that equation 25 is loosely a statement that the transition between flow regimes occurs at constant ratio of bouyancy to driving pressures, scaled by the aspect ratio of the medium:

$$\frac{L}{H}\frac{(\Delta\rho g)}{\frac{\partial P}{\partial x}\big|_{average}} = 2c \tag{28}$$

It is therefore expected that a plot of driving pressure against bouyancy force at the transitions between flow regimes will be linear, with gradient $\frac{L}{2cH}$ (figure 39).

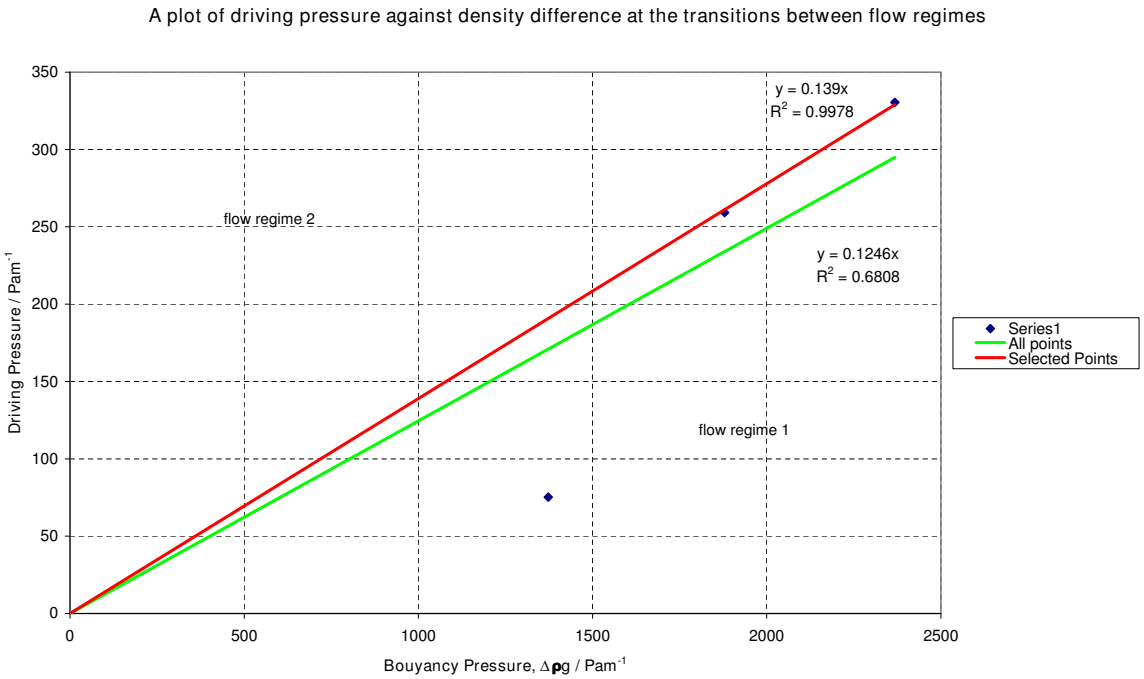

Figure 39: Linear regressions to plots of driving pressure gradient against bouyancy pressure. The green lines shows a regression based on all of the points, the red line only uses the two points at the highest density contrast, as the third point appears to be anomalously low.

It is clear that more data is needed to ensure transitions do occur at constant ratios of driving to bouyancy pressures. The large discrepancy in the transition observed at lowest density contrast may arise from the method of measuring the time of transition, which is subject to large errors as there may be some time lag between the change to a gravity dominated flow regime and the drop in concentrations observed in layer 3. Further experiments are needed to investigate this, using a range of bouyancy contrasts, and a fixed pressure gradient for each experiment (see §C.2), which should eliminate a lot of the errors in these measurements.

However, a very rough prediction of the flow regime expected in EOR can be made using the measured gradient from figure 39, and some typical values from Salt Creek. The gradient gives a value of $c = 10.7$, which for $L \approx 200$ m, and $L \approx 25$ m suggests that the transition occurs at a ratio of driving pressure to bouyancy pressure of 0.37. A density difference of 400 - 600 kgm^{-3} [O'Brien et al., 2010], and injection and production pressures of 15 MPa and 8 MPa, suggest that flow at Salt Creek is viscosity dominated, and therefore focussed down the high permeability layers in the reservoir (figure 40).

The regime developed is also likely to be affected by the permeability structure of the reservoir as this will affect the relative ease of progress in a horizontal or vertical direction. Large permeability changes with depth at Salt Creek are expected to inhibit vertical flow and further favour flow regime 2. However, no time was available in this

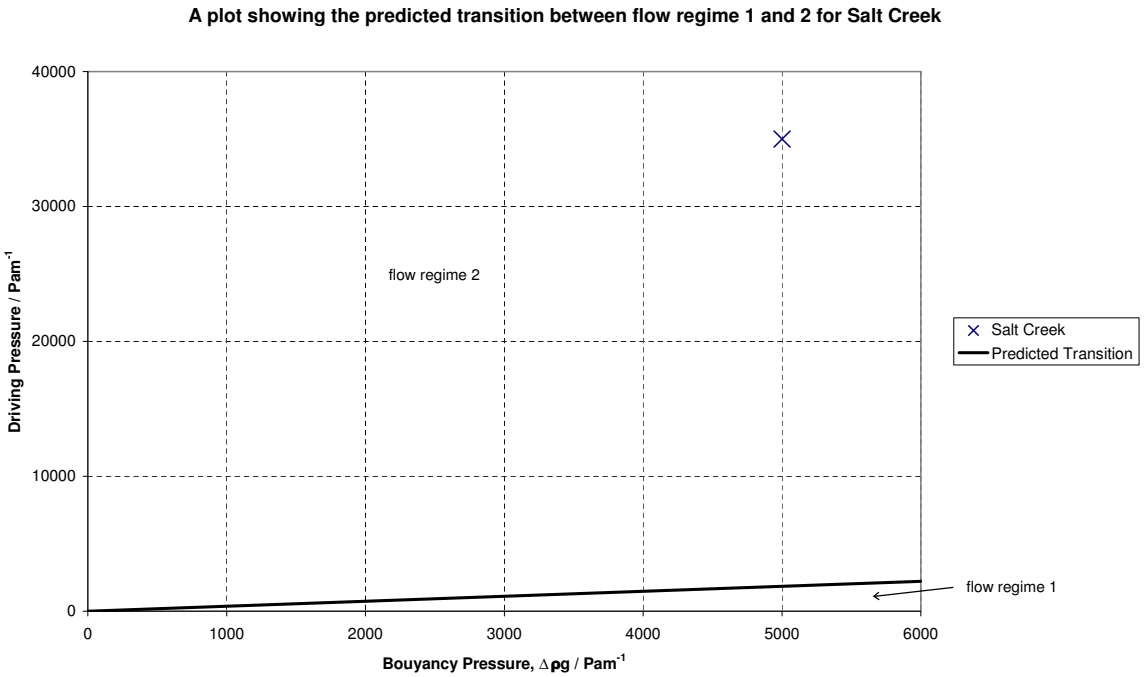

Figure 40: Plot showing the predicted transition pressures for the aspect ratio of the reservoir at Salt Creek, with approximate driving and bouyancy pressures acting in the reservoir.

project to investigate the effects of different permeability structures on the flow regime, and further experiments using varying permeability structures are suggested to investigate this.

6.4 Current Retreats at Sleipner

Late in the project it was noted that the retreat of the water current intruding the lower high permeability layer was similar to the shrinkage of approximately elliptical CO_2 horizons observed at the Sleipner injection experiment in the North Sea. Here CO_2 has been injected at the base of the Utsira Sand formation since 1996 [Baklid and Owren, 1996]. From here it flows upwards, stalling and spreading at 9 horizons believed to represent thin mud layers within the formation, before reaching Nordland Shale cap rock. The area of each horizon increases linearly with time [Bickle et al., 2007], consistent with a spreading axisymmetric gravity current with constant input flux [Lyle et al., 2005]. The deepest horizons (1 - 4) were found to stop growing and eventually shrink, accompanied by an overall decrease in amplitude that was concluded not to be solely due to acoustic attenuation [Boait et al., prep].

It is speculated that the shrinkage of these horizons occurs by a similar mechanism to the retreat of water from the lower high permeability layer described in §5.4.4. Unlike in the experiments, the pressure gradient driving the growth of the currents is caused by the gradient of the interface between the two fluids [Lyle et al., 2005]. If the layers are to

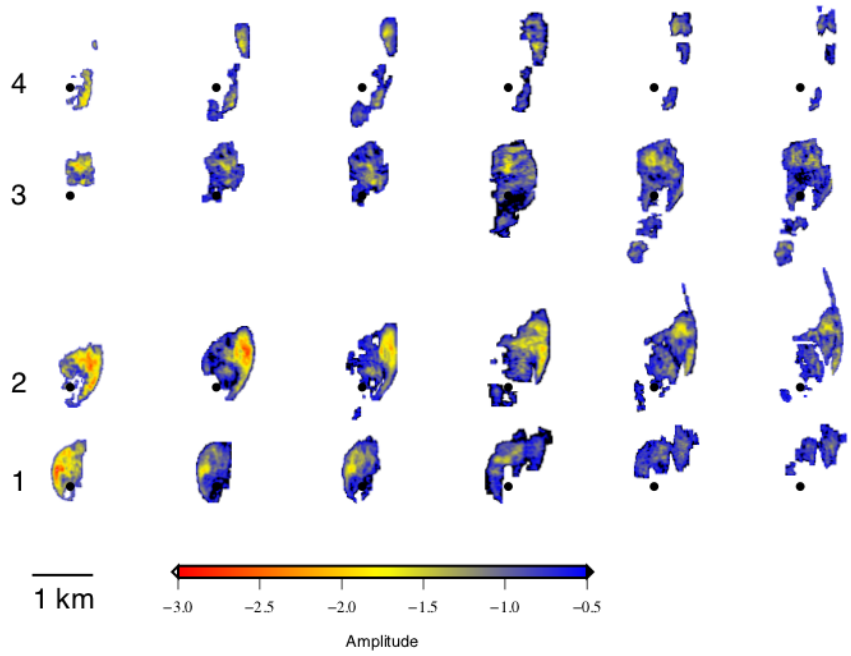

Figure 41: Horizontal slices through time-lapse seismic data showing amplitude variation for 1 - 4 horizons as function of time (see Figure 3 for vertical position of each horizon). Warmer and colder colors = stronger and weaker amplitudes; solid circle = injection point. Taken from Boait et al.

---

first grow, and then shrink under gravity, there must be some reduction in this driving pressure gradient.

As less dense fluid penetrates through a less permeable barrier, the flow established above the barrier tends to pull fluid through at an increasing rate [Neufeld and Huppert, 2009]. It is therefore speculated that flow of CO_2 through the mud layers may reduce the pressure driving the spread of the flow with time, allowing the horizons to retreat due to the gravitational instability of the wedges of less dense fluid. However, an understanding of the dynamical pressures acting in the CO_2 column would be necessary to show whether this is a viable mechanism for horizon shrinkage at Sleipner.

7 Conclusions

- Many of the aspects of flow observed in a heterogenous porous medium can be explained using a 1D analytical model in combination with a consideration of pressure gradients due to injection pressures and bouyancy forces.
- Override and channeling of the injected fluid due to viscosity and density contrasts causes faster advance of the injected fluids than expected from theory.
- Pressure gradients perpendicular to layers can be generated by differences in interface position between adjacent layers, when the injected and ambient fluids are of different viscosity. These are likely to be significant in EOR.
- These pressure gradients act to drive the growth of pore scale viscous fingers from advanced injected fluid fingers before breakthrough, greatly increasing the area of the interface between injected and ambient fluids, promoting mixing. Following breakthrough, these pressure gradients will act to drive the retreat of these pore scale fingers, reducing the surface area of the interface, and inhibiting mixing.
- Two different flow regimes are observed in a vertically orientated tank, with flow either focussed along high permeability layers, or along the top of the tank. The permeability focussed flow is expected to lead to most dissolution of CO_2 in EOR geometries, and is predicted to exist at the Salt Creek EOR project. Further experiments may be necessary to better quantify the transition between these flow regimes.
- Retreat of horizons observed at Sleipner may be explained by gravitational instability of CO_2 gravity currents that are less dense than the ambient reservoir brines.

Acknowledgements

I would like to thank my supervisors: Jerome Neufeld for help with experiments, maths and Matlab, Mike Bickle for providing geological context and back of the envelope calculations, and both of them for putting up with an erratic student. I would also like to thank Mark Hallworth for sharing his extensive experience with experimental design, and Madeleine Golding for guiding my first steps in Matlab.

References

[Alfredsson et al., 2008] Alfredsson, H., Hardason, B., Franzson, H., and S.R., G. (2008). CO_2 sequestration in basaltic rock at the Hellisheidi site in SW Iceland: stratigraphy and chemical composition of the rocks at the injection site. *Mineralogical Magazine*, 72(1):1–5.

[G.P.A., 1963] Glycerin Producers Association (1963). Physical properties of glycerine and its solutions.

[Bachu, 2008] Bachu, S. (2008). CO_2 storage in geological media: Role, means, status and barriers to deployment. *Progress in Energy and Combustion Science*, 34:254–273.

[Baklid and Owren, 1996] Baklid, A., K. R. and Owren, G. (1996). Sleipner Vest CO_2 disposal, CO_2 injection into a shallow underground aquifer. *Society of Petroleum Engineers*.

[Bear, 1972] Bear, J. (1972). *Dynamics of Fluids in Porous Media*. Dover Publications.

[Bickle, 2009] Bickle, M. (2009). Geological carbon storage. *Nature Geoscience*, 2(12):815–818.

[Bickle et al., 2007] Bickle, M., Chadwick, A., Huppert, H., Hallworth, M., and Lyle, S. (2007). Modelling carbon dioxide accumulation at sleipner: Implications for underground carbon storage. *Earth and Planetary Science Letters*, 255:164–176.

[Bickle et al., 2011] Bickle, M., Chapman, H., Galy, A., Kampman, N., Dubacq, B., Ballentine, C., and Zhou, Z. (2011). CO_2-brine-mineral reactions in geological carbon storage: Results from an EOR experiment. *AGU Abstract*.

[Boait et al., prep] Boait, F., White, N., Bickle, M., Chadwick, R., Neufeld, J., and Huppert, H. (in prep.). Spatial and temporal evolution of injected CO_2 at the Sleipner field, North Sea. *Journal of Geophysical Research*.

[Burke, 2011] Burke, L. (2011). Carbon dioxide fluid flow modeling and injectivity calculations. *US Geological Survey*.

[Cinar et al., 2006] Cinar, Y., Jessen, K., Berenblyum, R., Juanes, R., and Orr, F. J. (2006). An experimental and numerical investigation of crossflow effects in two-phase displacements. *Society of Petroleum Engineers*, 11(2):216–226.

[Gilfillan et al., 2008] Gilfillan, S., Ballentine, C., Holland, G., Blagburn, D., Sherwood Lollar, B., Stevens, S., Schoell, M., and Cassidy, M. (2008). The noble gas geochemistry of natural CO_2 gas reservoirs from the colorado plateau and rocky mountain provinces, usa. *Geochimica et Cosmochimica Acta*, 74:1174–1198.

[Grygar and Schmults, 2009] Grygar, B. and Schmults, E. (2009). Greenhouse gas emission reduction creation report for the Salt Creek enhanced oil recovery (EOR) project for CY 2008. Technical report, Howell Petroleum Corporation.

[Holt et al., 1995] Holt, T., Jensen, J., and Lindeberg, E. (1995). Underground storage of CO_2 in aquifers and oil reservoirs. *Energy Conversion and Management*, 36(6-9):535–538.

[Homsy, 1987] Homsy, G. (1987). Viscous fingering in porous media. *Annual Review of Fluid Mechanics*, 19:271–311.

[Huppert and Woods, 1995] Huppert, H. and Woods, A. (1995). Gravity-driven flows in porous layers. *Journal of Fluid Mechanics*, 292:55–69.

[Johnson and Santillo, 2003] Johnson, P. and Santillo, D. (2003). Carbon capture and sequestration: Potential environmental impacts.

[Kelemen and Matter, 2008] Kelemen, P. and Matter, J. (2008). In situ carbonation of peridotite for CO_2 storage. *Proceedings of the National Academy of Sciences*, 105(45):17295–17300.

[Lyle et al., 2005] Lyle, S., Huppert, H., Hallworth, M., Bickle, M., and Chadwick, A. (2005). Axisymmetric gravity currents in a porous medium. *Journal of Fluid Mechanics*, 543:293–302.

[Meyer, 2007] Meyer, J. (2007). Summary of carbon dioxide enhanced oil recovery (CO_2 EOR) injection well technology. Technical report.

[Neufeld et al., 2010] Neufeld, J., Hesse, M., Riaz, A., Hallworth, M., Tchelepi, H., and Huppert, H. (2010). Convective dissolution of carbon dioxide in saline aquifers. *Geophysical Research Letters*, 37:L22404.

[Neufeld and Huppert, 2009] Neufeld, J. and Huppert, H. (2009). Modelling carbon dioxide sequestration in layered strata. *Journal of Fluid Mechanics*, 625:353–370.

[O'Brien et al., 2010] O'Brien, J., Moran, J., Wilbourn, G., Morris, S., Andersen, J., and Quezada, O. (2010). Monitoring a CO_2 flood with fine time steps: Salt creek 4D. *The Leading Edge*, 29(8):912–919.

[Solomon et al., 2007] Solomon, S., Qin, D., Manning, M., Alley, R., Berntsen, T., Bindoff, N., Chen, Z., Chidthaisong, A., Gregory, J., Hegerl, G., Heimann, M., Hewitson, B., Hoskins, B., Joos, F., Jouzel, J., Kattsov, V., Lohmann, U., Matsuno, T., Molina, M., Nicholls, N., Overpeck, J., Raga, G., Ramaswamy, V., Ren, J., Rusticucci, M.,

Somerville, R., Stocker, T., Whetton, P., Wood, R., and Wratt, D. (2007). *Technical Summary. In: Climate Change 2007: The Physical Science Basis. Contribution of Working Group I to the Fourth Assessment Report of the Intergovernmental Panel on Climate Change*. Cambridge University Press, Cambridge, United Kingdom and New York, NY, USA.

[Strandkvist et al., prep] Strandkvist, C., Neufeld, J., and Huppert, H. (in prep.). The competition between gravity and flow-focusing in two-layered porous media. *Journal of Fluid Mechanics*.

[Weast, 1985] Weast, R. (1984-1985). *Handbook of Chemistry and Physics*. CRC Press, 65th edition.